Research paper

Modeling large deformations of thin-walled SMA structures by shell finite elements

Luka Porenta [a], Marko Lavrenčič [b], Jaka Dujc [b], Miha Brojan [a], Jaka Tušek [a], Boštjan Brank [b,*]

[a] *University of Ljubljana, Faculty of Mechanical Engineering, Aškerčeva 6, Ljubljana, 1000, Slovenia*
[b] *University of Ljubljana, Faculty of Civil and Geodetic Engineering, Jamova 2, Ljubljana, 1000, Slovenia*

A R T I C L E   I N F O

A B S T R A C T

Many shape memory alloy (SMA) applications, such as biomedical devices, electromechanical actuators, and elastocaloric cooling devices, are based on thin-walled flat or shell-like structures. An advanced design of such structures requires the development of an efficient and accurate numerical tool for simulations of very thin and curved SMA structures that may experience large deformations and even buckling upon thermo-mechanical loading. So far, finite element models for finite strain deformations of SMA structures have been based on 3D solid formulations, which are relatively inefficient for solving (thin) shell problems. In this paper, we present a finite element model for the analysis of shape memory alloy shells. Our model is based on a 7-parameter, large-rotation, one-director shell formulation, which takes into account a fully three-dimensional form of the constitutive equations for the isothermal transformations of isotropic superelasticity, as well as the shape-memory effect in a simplified way. In fact, we present three 4-node shell finite elements for SMAs. Two of them use the assumed natural strain concepts for the transverse shear strains, through-the-thickness normal strain, and membrane strains. The third element is a combination of the assumed natural strain and the enhanced assumed strain concepts, applied to satisfy the zero through-the-thickness-normal-stress condition for thin geometries to a high degree of accuracy. After a detailed description of the SMA finite element models for shells in the first part of the paper, numerical examples in the second part illustrate the approach. Compared to 3D solid SMA formulations, our results show excellent accuracy, even with a significantly reduced number of degrees of freedom, which consequently translates into a reduction in the computational time.

© 2021 The Authors. Published by Elsevier B.V.
This is an open access article under the CC BY license
(http://creativecommons.org/licenses/by/4.0/)

1. Introduction

Shape memory alloys (SMAs) belong to a group of smart materials that are characterized by a change in their properties when acted upon by external stimuli (stress and temperature for SMAs). Typically, SMAs are divided into Ni-Ti-based, Cu-based, and Fe-based groups, among which Ni-Ti is the most widely used in a large number of applications [1]. In medicine,

---

* Corresponding author.
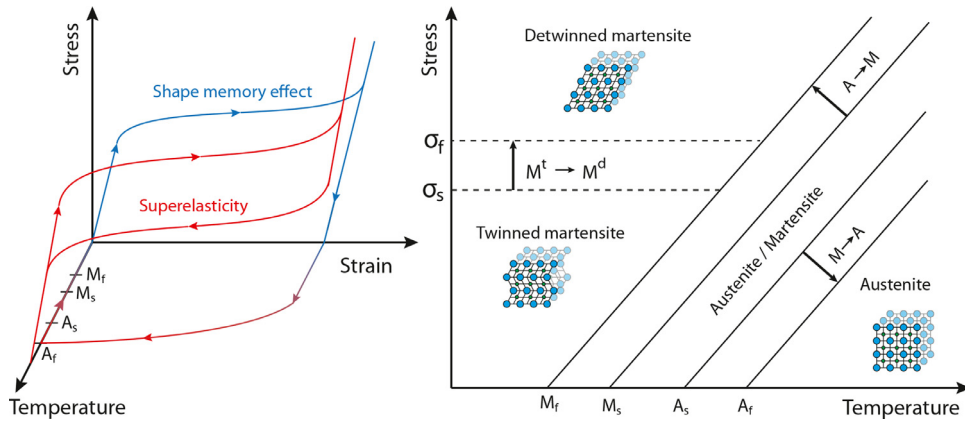   *E-mail address:* bbrank@fgg.uni-lj.si (B. Brank).

Fig. 1. Shape-memory effect and superelasticity (left). Phase diagram (right).
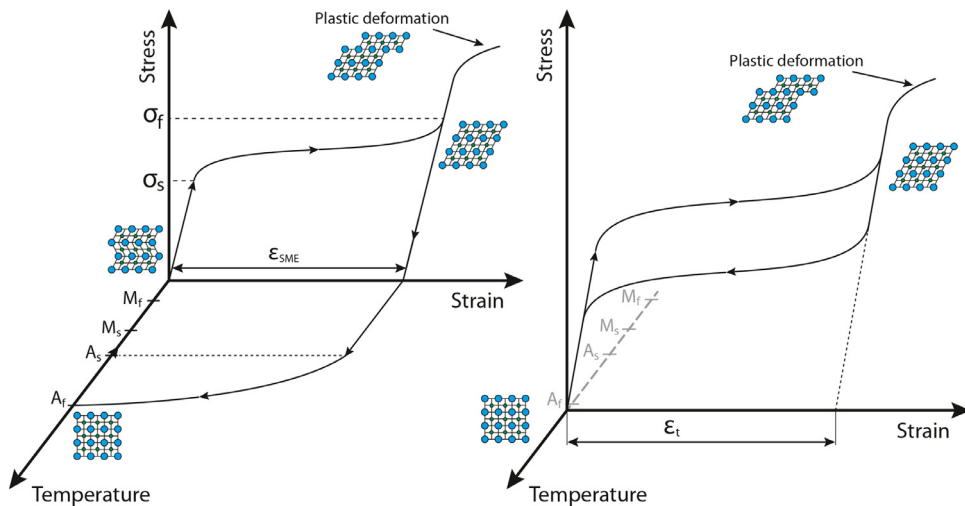

Fig. 2. Stress-strain-temperature diagram and crystal lattices: shape-memory effect (left) and superelasticity (right).

Ni–Ti is used for stents, surgical tools and bone implants due to its biocompatibility and comparable material properties with those of bone [2–4]. In robotics, SMAs are used as noise-free, small-size actuators with a large force-to-weight ratio [5]. In aeronautics, SMAs are employed for actuators, vibration-damping elements, seals, deployment mechanisms [6,7], and mor-phing wings [8]. In civil engineering, SMAs are used as seismic-response-control and damping elements [9]. Applications in energy and process engineering are also under intensive development [10,11], especially in elastocaloric cooling technology [12], due to its great potential as an alternative to vapor-compression refrigeration technology, which is relatively inefficient and still uses environmentally harmful refrigerants [13].

SMAs have two special properties, illustrated in Fig. 1 (left). First, the shape-memory effect (SME) is the ability to recover an initial shape after being deformed and subsequently subjected to high temperature, and second, superelasticity (SE) is the ability to recover from large deformations (up to 8%) without any permanent deformation. Both properties are attributed to the fact that SMAs are found in two different phases, see Fig. 1 (right): a low-temperature product phase called martensite (M) and a high-temperature parent phase called austenite (A). Because the crystal structure of A is highly symmetric, it exists in only one variant, while M can be found in many variants due to the lower symmetry of its crystal structure. Twinned or self-accommodated martensite M^t, which is stable at low stresses, occurs in different variants. At a critical stress σ_s the detwinned (or stress-induced) martensite M^d (the variant with the preferable orientation for a given stress state) occurs.

Figure 2 (left) shows the stress-strain-temperature diagram of the SME and the corresponding crystal lattices. When M is subjected to mechanical loading at low temperature, it deforms and the detwinning process occurs. On the macro-scale, this is a change of shape, while on the micro-scale, martensite variants occur that are preferable for the given stress state. During unloading, martensite variants do not change; therefore, pseudo-plastic deformation ε_{SME} is present at zero loads. Shape recovery occurs by subjecting the material to a temperature above the austenitic finish temperature A_f, where only A is stable. During a temperature increase, the phase transformation from M to A begins at the austenitic transformation start temperature A_s and finishes at A_f. On the other hand, cooling of a SMA causes a martensitic transformation (MT) with

the formation of self-accommodated martensite variants M^t. The transformation begins at the martensitic transformation's start temperature M_s and ends at the martensitic transformation's finish temperature M_f. In contrast to heating, cooling to its initial temperature does not cause any shape change (except the volume change due to thermal contraction). Shape recovery is possible if the deformation is not too large, otherwise, permanent plastic deformation occurs, as shown in Fig. 2.

Superelasticity (also called pseudoelasticity) is exhibited by a SMA when it is mechanically loaded and unloaded above the temperature A_f. A hysteresis occurs, as shown in Fig. 2 (right): while loading, stress-induced martensite M^d is formed during an exothermic MT (which is observed at the macroscopic level as a large deformation), and while unloading, an endothermic reverse MT from M to A takes place and the deformation vanishes. The mechanism is not elastic because the transformation, i.e., the change of the crystal lattice, occurs. The reversible deformation is limited by the maximum transformation strain ε_t. Depending on the strain rate and the heat exchange between the SMA and the environment, the SMA can heat up or cool down during the transformation, which is called the elastocaloric effect.

Numerous SMA material models have been developed, and these can be roughly grouped into three categories. Micro-models focus on phenomena such as grain nucleation and growth, detwinning, and reorientation [14,15]. Micro-macro-models combine microscopic features with macro-scale thermodynamics [16,17], while macro-models use thermodynamic variables to describe the macro-observed phenomena. Many of the macro-models describe superelasticity and the shape memory effect for small strains [18,19]. Some include tension-compression asymmetry based on a modified transformation limit function [20,21] and the difference between austenite and martensite material properties by a nonlinear order parameter [22]. To model detwinning and reorientation, a separate treatment of self-accommodated and stress-induced martensite is required, as well as a criterion for reorientation [23–26], while the effect of cyclic loading can be considered using an internal variable representing the accumulated martensite [27–29]. It is worth mentioning that not only has isothermal superelastic behavior been studied: temperature changes during a transformation were modeled by treating the released latent heat as a volume heat source [30–32].

The finite strain macro-models are often an extension of the small strain formulations, see, e.g., [33–35]. They apply a multiplicative decomposition of the deformation gradient $\boldsymbol{F}$, e.g., [33,36]. One of the first finite strain SMA models was proposed by Lubliner and Auricchio [37,38]. Some models decompose $\boldsymbol{F}$ into several parts, i.e., elastic, transformation and plastic [39], elastic, transformation and thermal [40], or elastic and transformation, with the latter further divided into a recoverable and plastic part (that accounts for the dissipation during the transformation and not for plastic deformations) [41]. Heat generation during the transformation (due to latent-heat release) was considered in, e.g., [42–44], compression-tension asymmetry in, e.g., [42,45], detwinning and reorientation in, e.g., [46,47], and anisotropy due to crystallographic texture in, e.g., [45,48,49]. The shape memory effect and superelastic response, without using the martensite volume fraction as an internal variable, were studied in [36,50,51], and the effects due to cyclic loading were considered in, e.g., [52,53].

The main motivation for our work stems from the need for an accurate prediction of the response of mechanically loaded SMA structures, which could be applied in elastocaloric devices. Obviously, thin-walled structures are preferable as they enable the rapid (efficient) transfer of heat [54]. Currently, the macroscopic SMA material models have been implemented almost exclusively into 3D solid finite elements, which can be very inefficient for the modeling of thin structures. To the best of our knowledge, there have been only a few SMA formulations devised for structural elements; e.g., in [55] for plates, in [56,57] for membranes, in [58] for solid-beams, and in [59] for a small strain corotational shell formulation. There have been no attempts to combine a finite strain SMA material model with a shell finite element formulation, although it is well known that solid finite elements can be very inaccurate when representing the bending of thin-walled structures. For this reason, it seems rational to focus on the development of shell finite element formulations for the simulation of thin and curved SMA structures, especially because there exist thin-walled formulations that can incorporate fully 3D constitutive models. Let us mention 7-parameter (7-p) shells and solid-shells (e.g. [60]), the latter being rotation-free that simplify computer implementation.

The main focus of this work is combining the finite strain SMA material model with the 7-p shell finite element model. To this end, three 7-p, 4-node, shell finite element formulations were designed with the extensive use of the assumed natural strain (ANS) concepts that were originally developed for 5-parameter shell formulations. In particular, our 7-p formulation that is called 2ANS uses the ANS concepts for the transverse-shear strains [61] and the through-the-thickness stretching [62]. The 7-p formulation that is called 3ANS additionally uses the ANS concept for the membrane strains, in particular, the approach that was proposed in [63] and extensively tested in [63–66], is adopted. The membrane ANS makes the 3ANS formulation low-sensitive to mesh distortion. The third 7-p shell formulation is a combination of the ANS and the enhanced assumed-strain (EAS) concepts designed to better enforce the zero-through-the-thickness-normal-stress condition for thin SMAs, with respect to the 2ANS and 3ANS formulations. It must be emphasized that the resulting 7-p shell finite element formulations are a much better choice than the solid finite element formulations for the numerical simulations of very thin and curved SMA structures that can undergo large deformations, large rotations, and buckling, an understanding of which is an interest for some SMA applications, e.g., seismic applications and elastocaloric cooling technology.

The rest of the text is organized in the following way. Section 2 revises the finite strain SMA material model from [35,36]. The focus is on an effective solution procedure for local systems of equations when performing an update of the internal variables. In Section 3, the 7-p shell finite element formulations are presented. In Section 4, numerical examples illustrate the capability of the derived formulation, and the conclusions are drawn in Section 5.

2. Finite strain constitutive model for SMA

2.1. Continuous framework

In this section we revise the 3D constitutive model for a SMA that was originally presented by Souza et al. [50] for small strains and later extended to finite strains by Evangelista et al. [35] and Arghavani et al. [36].

2.1.1. Model development

For a deformable body, the deformation gradient $\boldsymbol{F}$, $\det \boldsymbol{F} = J > 0$, can be decomposed with polar decomposition as $\boldsymbol{F} = \boldsymbol{R}\boldsymbol{U} = \boldsymbol{V}\boldsymbol{R}$, where $\boldsymbol{U}$ and $\boldsymbol{V}$ are the symmetric positive definite right and left stretch tensors, respectively, and $\boldsymbol{R}$ is a proper orthogonal rotation tensor. The right Cauchy-Green deformation tensor and the Green-Lagrange strain tensor are:

$$\boldsymbol{C} = \boldsymbol{F}^{\mathrm{T}} \boldsymbol{F}, \quad \boldsymbol{E} = \frac{1}{2}(\boldsymbol{C} - \boldsymbol{1}), \tag{1}$$

where $\boldsymbol{1}$ is the identity tensor. Similar to the finite-strain plasticity [67], a multiplicative decomposition of $\boldsymbol{F}$ into elastic $\boldsymbol{F}_e$ and transformation $\boldsymbol{F}_t$ parts is postulated:

$$\boldsymbol{F} = \boldsymbol{F}_e \boldsymbol{F}_t \tag{2}$$

that introduces the initial (i.e., undeformed), intermediate (i.e., transformed) and current (i.e., deformed) configurations. Furthermore, the elastic right Cauchy-Green deformation tensor $\boldsymbol{C}_e$ and the transformation right Cauchy-Green deformation tensor $\boldsymbol{C}_t$ can be defined with respect to the intermediate and reference configurations as:

$$\boldsymbol{C}_e = \boldsymbol{F}_e^{\mathrm{T}} \boldsymbol{F}_e, \quad \boldsymbol{C}_t = \boldsymbol{F}_t^{\mathrm{T}} \boldsymbol{F}_t \tag{3}$$

and Eqs. (1)$_1$, (2), and (3)$_1$ can be used to relate $\boldsymbol{C}_e$ with $\boldsymbol{C}$ as:

$$\boldsymbol{C} = \boldsymbol{F}^{\mathrm{T}} \boldsymbol{F} = \boldsymbol{F}_t^{\mathrm{T}} \boldsymbol{F}_e^{\mathrm{T}} \boldsymbol{F}_e \boldsymbol{F}_t \Rightarrow \boldsymbol{C}_e = \boldsymbol{F}_t^{-\mathrm{T}} \boldsymbol{C} \boldsymbol{F}_t^{-1}. \tag{4}$$

It turns out to be useful to define the velocity gradient tensor $\boldsymbol{L} = \dot{\boldsymbol{F}} \boldsymbol{F}^{-1}$ and the symmetric and skew-symmetric parts of $\boldsymbol{L}$ that are the rate of the deformation tensor $\boldsymbol{d} = \frac{1}{2}(\boldsymbol{L} + \boldsymbol{L}^{\mathrm{T}})$ and the vorticity tensor $\boldsymbol{w} = \frac{1}{2}(\boldsymbol{L} - \boldsymbol{L}^{\mathrm{T}})$. With respect to the dot denoting the time derivative, it is worth noting that for time-independent material models, such as the one considered here, the notion "time" is used for the loading parameter that linearly increases/decreases the level of the external loading. The relation between $\boldsymbol{d}$ and the time derivative of the Green-Lagrange tensor $\dot{\boldsymbol{E}}$ (i.e., the strain rate) can be obtained by using $\boldsymbol{L}$ as (see Eq. (A.1) in Appendix):

$$\dot{\boldsymbol{E}} = \frac{1}{2}\dot{\boldsymbol{C}} = \boldsymbol{F}^{\mathrm{T}} \boldsymbol{d} \boldsymbol{F}. \tag{5}$$

According to the experimental results, the transformation is (almost) isochronic, which is expressed by $\det \boldsymbol{F}_t = 1$. Taking the time derivative gives $\mathrm{tr}\, \boldsymbol{d}_t = 0$ (see Eq. (A.2) in Appendix), where $\boldsymbol{d}_t = \frac{1}{2}(\boldsymbol{L}_t + \boldsymbol{L}_t^{\mathrm{T}})$ and $\boldsymbol{L}_t = \dot{\boldsymbol{F}}_t \boldsymbol{F}_t^{-1}$.

The Helmholtz free energy ψ must depend on $\boldsymbol{F}_e$ only through the elastic right Cauchy-Green deformation tensor $\boldsymbol{C}_e$, because of the material objectivity. It is assumed that ψ can be additively split into the elastic ψ_e and transformation parts ψ_t, and that the latter depends on the transformation Green-Lagrange deformation tensor $\boldsymbol{E}_t = \frac{1}{2}(\boldsymbol{C}_t - \boldsymbol{1})$ (which plays the role of the internal variable) and temperature T:

$$\psi = \psi(\boldsymbol{C}_e, \boldsymbol{E}_t, T) = \psi_e(\boldsymbol{C}_e) + \psi_t(\boldsymbol{E}_t, T). \tag{6}$$

Moreover, let ψ be valid for both the austenite and martensite phases. For an isotropic SMA, the hyperelastic strain-energy function $\psi_e(\boldsymbol{C}_e)$ can be expressed by the invariants of $\boldsymbol{C}_e$ as $\psi_e(\boldsymbol{C}_e) = \psi_e(I_{\boldsymbol{C}_e}, II_{\boldsymbol{C}_e}, III_{\boldsymbol{C}_e})$. Let us choose the following strain-energy function of the neo-Hookean type:

$$\psi_e(\boldsymbol{C}_e) = \frac{1}{2}\mu (I_{\boldsymbol{C}_e} - 3 - \log III_{\boldsymbol{C}_e}) + \frac{1}{4}\lambda (III_{\boldsymbol{C}_e} - 1 - \log III_{\boldsymbol{C}_e}), \tag{7}$$

where μ and λ are Lams coefficients. Because $III_{\boldsymbol{C}_e} = \det \boldsymbol{C}_e = \det(\boldsymbol{C}\boldsymbol{C}_t^{-1})$, see Eq. (4), and $I_{\boldsymbol{C}_e} = \mathrm{tr}\boldsymbol{C}_e = \mathrm{tr}(\boldsymbol{F}_t^{-\mathrm{T}} \boldsymbol{C} \boldsymbol{F}_t^{-1}) = \mathrm{tr}(\boldsymbol{C}\boldsymbol{F}_t^{-1}\boldsymbol{F}_t^{-\mathrm{T}}) = \mathrm{tr}(\boldsymbol{C}\boldsymbol{C}_t^{-1})$, the strain-energy function (Eqs. (7) and (6)) can be rewritten in terms of the tensors from the reference configuration

$$\psi_e(\boldsymbol{C}_e) = \tilde{\psi}_e(\boldsymbol{C}, \boldsymbol{C}_t) \quad \text{and} \quad \psi(\boldsymbol{C}_e, \boldsymbol{E}_t, T) = \tilde{\psi}(\boldsymbol{C}, \boldsymbol{C}_t, T). \tag{8}$$

The transformation part ψ_t of the Helmholz free energy is chosen after [36] as:

$$\psi_t(\boldsymbol{E}_t, T) = \tau_M(T)\,||\boldsymbol{E}_t|| + \frac{1}{2}\bar{h}\,||\boldsymbol{E}_t||^2 + \mathscr{I}(||\boldsymbol{E}_t||), \tag{9}$$

where $\tau_M(T)$ provides the temperature dependency of the material response

$$\tau_M(T) = \beta\,\langle T - T_0 \rangle, \tag{10}$$

$\bar{h}$ is the material-hardening parameter due to the transformation, β is a material parameter related to the dependence of the critical stress on the temperature, and $T_0 = M_f$. Furthermore, the Macaulay bracket used here is defined as $\langle x \rangle = \frac{x - |x|}{2}$, and the norm in Eq. (9) is given as $||\boldsymbol{A}|| = \sqrt{\boldsymbol{A} : \boldsymbol{A}} = \sqrt{\mathrm{tr}(\boldsymbol{A}\boldsymbol{A}^{\mathsf{T}})}$. The indicator function $\mathscr{I}(||\boldsymbol{E}_t||)$ in Eq. (9)

$$\mathscr{I}(||\boldsymbol{E}_t||) = \begin{cases} 0 & ||\boldsymbol{E}_t|| \leq \varepsilon_L \\ \infty & \text{otherwise} \end{cases} \tag{11}$$

handles the constraint on the transformation strain norm

$$||\boldsymbol{E}_t|| \leq \varepsilon_L, \tag{12}$$

where ε_L is another parameter of the material model linked to the maximum transformation strain norm at the end of the phase transformation. The indicator function states that the violation of inequality (12) is inadmissible.

The Clausius-Duhem inequality of the second law of thermodynamics states the following:

$$\mathscr{D} = \boldsymbol{S} : \frac{1}{2}\dot{\boldsymbol{C}} - (\dot{\psi} + \eta \dot{T}) \geq 0, \tag{13}$$

where $\boldsymbol{S}$ is the second Piola-Kirchhoff stress tensor and η is the entropy. By inserting Eq. (6) into Eq. (13), we obtain:

$$\mathscr{D} = \underbrace{\boldsymbol{S} : \frac{1}{2}\dot{\boldsymbol{C}} - \frac{\partial \psi_e}{\boldsymbol{C}_e} : \dot{\boldsymbol{C}}_e}_{\textcircled{1}} - \underbrace{\frac{\partial \psi_t}{\boldsymbol{E}_t} : \dot{\boldsymbol{E}}_t}_{\textcircled{2}} - \underbrace{\frac{\partial \psi_t}{T} : \dot{T} - \eta \dot{T}}_{\textcircled{3}} \geq 0. \tag{14}$$

Let us elaborate on the expression labeled by $\textcircled{1}$. The time derivative of $\dot{\boldsymbol{C}}_e$ can be obtained by using Eq. (4) and the relation $\boldsymbol{L}_t^{-\mathsf{T}} = -\boldsymbol{L}_t^{\mathsf{T}}$ (see Eq. (A.3) in Appendix):

$$\dot{\boldsymbol{C}}_e = -\boldsymbol{L}_t^{\mathsf{T}}\boldsymbol{C}_e + \boldsymbol{F}_t^{-T}\dot{\boldsymbol{C}}\boldsymbol{F}_t^{-1} - \boldsymbol{C}_e\boldsymbol{L}_t. \tag{15}$$

Inserting Eq. (15) into $\textcircled{1}$ yields (see Eq. (A.4) in Appendix):

$$\boldsymbol{S} : \frac{1}{2}\dot{\boldsymbol{C}} - \frac{\partial \psi_e}{\boldsymbol{C}_e} : \dot{\boldsymbol{C}}_e = \underbrace{\left(\boldsymbol{S} - 2\boldsymbol{F}_t^{-1}\frac{\partial \psi_e}{\boldsymbol{C}_e}\boldsymbol{F}_t^{-T}\right) : \frac{1}{2}\dot{\boldsymbol{C}}}_{\boxed{1}} + \underbrace{2\boldsymbol{C}_e\frac{\partial \psi_e}{\boldsymbol{C}_e} : \boldsymbol{L}_t}_{\boxed{2}}. \tag{16}$$

For an elastic isothermal case, where $\mathscr{D} = 0$ and there is no change in transformation, the expression for the stress tensor and entropy follow from Eq. (14) and Eq. (16) as:

$$\mathcal{D} = 0, \dot{\boldsymbol{E}}_t = \boldsymbol{L}_t = \boldsymbol{0} \Rightarrow \begin{cases} \boldsymbol{S} = & 2\boldsymbol{F}_t^{-1}\frac{\partial \psi_e}{\boldsymbol{C}_e}\boldsymbol{F}_t^{-T} \\ \eta = & -\frac{\partial \psi_t}{T} \end{cases} \tag{17}$$

Because of Eq. (4), we can conclude that

$$\boldsymbol{F}_t^{-1}\frac{\partial \psi_e}{\boldsymbol{C}_e}\boldsymbol{F}_t^{-T} = \frac{\partial \tilde{\psi}_e}{\boldsymbol{C}} \Rightarrow \boldsymbol{S} = 2\frac{\partial \tilde{\psi}_e}{\boldsymbol{C}}. \tag{18}$$

It is assumed that the relations (17) are also valid in the case of a transformation that remains to be considered. To this end, let us introduce the back-stress tensor $\boldsymbol{X} = \frac{\partial \psi_t}{\boldsymbol{E}_t}$ and examine the part of the expression (14), labelled with $\textcircled{2}$ (see Eq. (A.5) in Appendix):

$$\begin{aligned} \boldsymbol{X} &= \tau_M(T)\frac{\partial ||\boldsymbol{E}_t||}{\boldsymbol{E}_t} + \frac{1}{2}h\frac{\partial ||\boldsymbol{E}_t||^2}{\boldsymbol{E}_t} + \frac{\partial \mathscr{I}(||\boldsymbol{E}_t||)}{\boldsymbol{E}_t} \\ &= h\boldsymbol{E}_t + (\tau_M(T) + \gamma)\boldsymbol{N}, \end{aligned} \tag{19}$$

where $\boldsymbol{N} = \frac{\boldsymbol{E}_t}{||\boldsymbol{E}_t||}$ and γ is a sub-differential of the indicator function $\partial \mathscr{I}(||\boldsymbol{E}_t||)$:

$$\gamma = \begin{cases} \geq 0 & ||\boldsymbol{E}_t|| = \varepsilon_L \\ 0 & ||\boldsymbol{E}_t|| < \varepsilon_L. \\ \text{undefined} & \text{otherwise} \end{cases} \tag{20}$$

The back-stress tensor $\boldsymbol{X}$ depends on the temperature (for $T > M_f$) and the transformation strain tensor. The parameter γ controls the end of the phase transformation and ensures the elastic response of the martensite after a full transformation. By using Eqs. (16), (17) and (19) in (14), the inelastic dissipation for the case of transformation can be expressed as:

$$\mathscr{D}_t = \underbrace{2\boldsymbol{C}_e\frac{\partial \psi_e}{\boldsymbol{C}_e}}_{\boldsymbol{P}} : \boldsymbol{L}_t - \boldsymbol{X} : \dot{\boldsymbol{E}}_t > 0. \tag{21}$$

The product $X : \dot{E}_t$ in (21) can be further manipulated by using (5) and the relation $\mathrm{tr}(AB) = \mathrm{tr}(BA)$ to obtain $X : \dot{E}_t = F_t X F_t^{\mathrm{T}} : d_t$. The decomposition $L_t = d_t + w_t$ and the symmetry of P result in $P : w_t = 0$ (because w_t is skew-symmetric), therefore the following holds $P : L_t = P : d_t$. These allow us to rewrite the dissipation inequality (21) as:

$$\mathscr{D}_t = P : d_t - \underbrace{F_t X F_t^{\mathrm{T}}}_{K} : d_t = \underbrace{(P - K)}_{Z} : d_t > 0. \tag{22}$$

By further introducing a transformation function $f(Z) \le 0$ (with its proposal left open for now) and assuming that the transformation case corresponds to the stress state giving $f(Z) = 0$, the evolution equation for the transformation case can be obtained. We postulate that among all the admissible states of transformation, we choose the one that renders the maximum dissipation $\mathscr{D}_t$ or the minimum of $-\mathscr{D}_t$. Recasting the original problem into the unconstrained minimization problem is possible by using the method of Lagrangian multipliers with the Lagrangian function defined as:

$$\mathscr{L}(Z, \dot{\zeta}) = -\mathscr{D}_t(Z) + \dot{\zeta} f(Z), \tag{23}$$

where $\dot{\zeta}$ is the Lagrange multiplier. In order to find the minimum of $\mathscr{L}(Z, \dot{\zeta})$, the stationarity, primal feasibility, dual feasibility and complementary slackness conditions must hold:

$$\frac{\partial \mathscr{L}(Z, \dot{\zeta})}{Z} = 0, \quad f(Z) \le 0, \quad \dot{\zeta} \ge 0, \quad \dot{\zeta} f(Z) = 0. \tag{24}$$

From the stationarity condition $(24)_1$, the evolution equation for the rate of transformation deformation d_t is obtained:

$$-d_t + \dot{\zeta} \frac{\partial f(Z)}{Z} = 0 \Rightarrow d_t = \dot{\zeta} \frac{\partial f(Z)}{Z}. \tag{25}$$

Let us choose the following expression for the transformation function (after [35,36]), which is similar to the classic yield functions for metals:

$$f(Z) = ||Z^{\mathrm{D}}|| - R, \tag{26}$$

where $Z^{\mathrm{D}} = (P - K)^{\mathrm{D}}$ is a deviatoric part of Z and the material parameter R defines the radius of the elastic domain and has a similar role as the yield stress in plasticity. By further using the relation for the symmetric tensor $\frac{\partial ||A||}{A} = \frac{A}{||A||}$, Eq. (25) yields the following evolution equation:

$$d_t = \dot{\zeta} \frac{Z^{\mathrm{D}}}{||Z^{\mathrm{D}}||}, \tag{27}$$

which completes the list of the basic equations for the considered SMA material model.

2.1.2. Equations in the reference configuration

To have the equations of the SMA material model given with respect to the reference configuration, the evolution Eq. (27) must be recast in terms of C and $E_t = \frac{1}{2}(C_t - 1)$ (or yet C_t), which is the internal variable. To this end, we use the procedure from Eqs. (5) and (27) to obtain the equality:

$$\dot{C}_t = 2 F_t^{\mathrm{T}} d_t F_t = 2 F_t^{\mathrm{T}} \dot{\zeta} \frac{Z^{\mathrm{D}}}{||Z^{\mathrm{D}}||} F_t = 2 \dot{\zeta} F_t^{\mathrm{T}} \frac{(P - K)^{\mathrm{D}}}{||(P - K)^{\mathrm{D}}||} F_t. \tag{28}$$

In order to facilitate the expression (28), let us first investigate $F_t^{\mathrm{T}} (P - K) F_t$ to obtain (see Eq. (A.6) in Appendix):

$$F_t^{\mathrm{T}} (P - K) F_t = F_t^{\mathrm{T}} P F_t - F_t^{\mathrm{T}} K F_t = Y C_t, \tag{29}$$

where the non-symmetric stress like tensor Y was introduced as:

$$Y = C S - C_t X. \tag{30}$$

Now, the term $F_t^{\mathrm{T}} (P - K)^{\mathrm{D}} F_t$ can be manipulated to obtain (see Eq. (A.7) in Appendix):

$$F_t^{\mathrm{T}} (P - K)^{\mathrm{D}} F_t = Y^{\mathrm{D}} C_t, \tag{31}$$

that finally leads to:

$$Z^{\mathrm{D}} = (P - K)^{\mathrm{D}} = F_t^{-\mathrm{T}} Y^{\mathrm{D}} F_t^{\mathrm{T}}. \tag{32}$$

Taking advantage of the symmetry of $Y^{\mathrm{D}} C_t$, the norm $||(P - K)^{\mathrm{D}}||$ is (see Eq. (A.8) in Appendix):

$$||Z^{\mathrm{D}}|| = ||(P - K)^{\mathrm{D}}|| = ||F_t^{-\mathrm{T}} Y^{\mathrm{D}} F_t^{\mathrm{T}}|| = \sqrt{Y^{\mathrm{D}} : Y^{\mathrm{D}^{\mathrm{T}}}} \ne ||Y^{\mathrm{D}}||. \tag{33}$$

Therefore, in the view of the above, the evolution Eq. (28) for $\dot{C}_t$ can be written as:

$$\dot{C}_t = 2 \dot{\zeta} \frac{Y^{\mathrm{D}}}{\sqrt{Y^{\mathrm{D}} : Y^{\mathrm{D}^{\mathrm{T}}}}} C_t = 2 \dot{\zeta} A C_t, \tag{34}$$

from where the definition of the non-symmetric tensor $\boldsymbol{A}$ is obvious. The transformation function (26) and Kuhn-Tucker conditions (24) can also be rewritten in terms of $\boldsymbol{Y}$ as:

$$f(\boldsymbol{Y}) = \sqrt{\boldsymbol{Y}^{\mathrm{D}} : \boldsymbol{Y}^{\mathrm{D}^{\mathrm{T}}}} - R, \tag{35}$$

$$f(\boldsymbol{Y}) \le 0, \quad \dot{\zeta} \ge 0, \quad \dot{\zeta} f(\boldsymbol{Y}) = 0. \tag{36}$$

The temperature effects in the material are linked with the back stress $\boldsymbol{X}$ and therefore with the tensor $\boldsymbol{N}$, see Eq. (19), which is the consequence of the choice for the transformation part of the free energy (9). The temperature effects should also be taken into account in the elastic case; however, $\boldsymbol{N}$ is undefined for $\boldsymbol{E}_t = \boldsymbol{0}$, which calls for an approximation of $\boldsymbol{N}$ for the elastic case. To this end, we can consider Eq. (34) during nucleation (i.e., at beginning of the forward phase transformation), which yields (assuming $\boldsymbol{X} = \boldsymbol{0}$)

$$\dot{\boldsymbol{E}}_t = \dot{\zeta} \, \frac{(\boldsymbol{C}\boldsymbol{S}_{el})^{\mathrm{D}}}{\sqrt{(\boldsymbol{C}\boldsymbol{S}_{el})^{\mathrm{D}} : (\boldsymbol{C}\boldsymbol{S}_{el})^{\mathrm{D}^{\mathrm{T}}}}}, \tag{37}$$

which indicates that during nucleation $\boldsymbol{E}_t$ evolves in the direction of $(\boldsymbol{C}\boldsymbol{S}_{el})^{\mathrm{D}}$. Here, $\boldsymbol{S}_{el} = \boldsymbol{S}(\boldsymbol{C}_t = \boldsymbol{1})$. Following [36], we adopt the direction (37) for all the elastic states. Thus, $\boldsymbol{N}$ is redefined for computational purposes as:

$$\boldsymbol{N} = \begin{cases} \frac{(\boldsymbol{C}\boldsymbol{S}_{el})^{\mathrm{D}}}{||(\boldsymbol{C}\boldsymbol{S}_{el})^{\mathrm{D}}||} & \text{if} \quad ||\boldsymbol{E}_t|| = 0 \\ \frac{\boldsymbol{E}_t}{||\boldsymbol{E}_t||} & \text{if} \quad ||\boldsymbol{E}_t|| \ne 0 \end{cases}. \tag{38}$$

2.2. Discrete framework

In the finite-element inelasticity, the solution in time is advanced through a sequence of discrete time points, $t_0, ..., t_n, t_{n+1}, ..., t_{end}$. Because of the single-step integration method, it suffices to focus on the generic increment from t_n to t_{n+1}. In our case, the central problem is: given the values of the state variables at t_n, i.e., $\boldsymbol{C}(t_n) = \boldsymbol{C}_n$ and $\boldsymbol{C}_t(t_n) = \boldsymbol{C}_{t,n}$, find their (converged) values at t_{n+1}, i.e. $\boldsymbol{C}_{n+1}$ and $\boldsymbol{C}_{t,n+1}$, by taking into account the constraint (12). To that end, the implicit methods to solve the evolution equation for $\boldsymbol{C}_{t,n+1}$ and the equilibrium equations for $\boldsymbol{C}_{n+1}$ are combined with the Newton-Raphson iterative method. The operator-split method is used to simplify the computation of the central problem. The update of $\boldsymbol{C}_{t,n+1}$ for a given value of $\boldsymbol{C}_{n+1}^{(i)}$ is followed by the update of the latter for the given value of the former.

The update of $\boldsymbol{C}_{t,n+1}$ takes place at Gauss integration points, while the update of $\boldsymbol{C}_{n+1}^{(i)}$ requires a consistent tangent operator and an assembly of the finite-element contributions into a global, non-linear system of equations, with the nodal generalized displacements as the unknowns. The index (i) denotes an iteration related to the global system.

2.2.1. Computations at the Gauss point

To integrate the evolution Eq. (34), we use the exponential mapping approximation, see, e.g., [68], which algorithmically conserves the inelastic volume (i.e., preserves $\det\boldsymbol{C}_t = \det\boldsymbol{F}_t = 1$) as required by the SMA model. For a given system of the first-order differential equations $\dot{\boldsymbol{y}} = \boldsymbol{G}(\boldsymbol{y})\boldsymbol{y}$, the exponential approximation leads to $\boldsymbol{y}_{n+1} = \exp((t_{n+1} - t_n)\,\boldsymbol{G}_{n+1})\boldsymbol{y}_n$. By applying this formula to Eq. (34), we obtain:

$$\boldsymbol{C}_{t,n+1} = \exp(2\,\zeta_{n+1}\boldsymbol{A}_{n+1}^{(i)})\,\boldsymbol{C}_{t,n}, \tag{39}$$

where $\zeta_{n+1} = (t_{n+1} - t_n)\,\dot{\zeta}$. The index (i) indicates that the current iterative value for $\boldsymbol{C}_{n+1}^{(i)}$ (which is the input for the Gauss-point update) is used to compute $\boldsymbol{A}_{n+1}^{(i)}$. By using the relations $\exp(\boldsymbol{A})^{-1} = \exp(-\boldsymbol{A})$ and $\exp(\boldsymbol{A})^{\mathrm{T}} = \exp(\boldsymbol{A}^{\mathrm{T}})$, and the symmetry of $\boldsymbol{C}_t$, we can replace Eq. (39) with

$$\boldsymbol{C}_{t,n+1}^{-1} = \exp\left(-2\,\zeta_{n+1}\boldsymbol{A}_{n+1}^{(i),\mathrm{T}}\right)\boldsymbol{C}_{t,n}^{-1}. \tag{40}$$

We compute the asymmetric matrix exponent in Eq. (40) as proposed in [69,70].

A Gauss-point update starts with the evaluation of the trial state, which is obtained by keeping the transformation flow frozen, i.e., $\boldsymbol{C}_{t,n+1}^{tr} = \boldsymbol{C}_{t,n}$. With these values and given $\boldsymbol{C}_{n+1}^{(i)}$, the trial stresses $\boldsymbol{S}_{n+1}^{tr}$ and $\boldsymbol{Y}_{n+1}^{tr}$ are computed. The trial state is a natural way to check the loading/unloading conditions. The elastic loading, unloading (or neutral loading) are simply verified if the nucleation/completion criterion (given below) during the trial state is satisfied, which enforces $\zeta_{n+1}^{tr} = 0$. In that case, the step is elastic. In the opposite case, inelastic loading is the result, and we need to compute the updated values of $\boldsymbol{C}_{t,n+1}$ and the parameters ζ_{n+1} and γ_{n+1}, which will enforce the consistency. The computation of the admissible state variables is given in terms of a set of non-linear equations with $\boldsymbol{C}_{t,n+1}$, ζ_{n+1} and γ_{n+1} as the unknowns.

For the inelastic step, there are two possibilities: the unsaturated state where $||\boldsymbol{E}_t|| < \varepsilon_L$, and the saturated state where $||\boldsymbol{E}_t|| = \varepsilon_L$. As a consequence, two sets of equations are generated. For the unsaturated state, the following system (labelled hereinafter as PT1)

$$\boldsymbol{R}_{\boldsymbol{C}_t, n+1} = \boldsymbol{C}_{t,n+1}^{-1} - \exp\left(-2\,\zeta_{n+1}\boldsymbol{A}_{n+1}^{(i),\mathrm{T}}\right)\boldsymbol{C}_{t,n}^{-1} = \boldsymbol{0}, \tag{41}$$

$$R_{\zeta,n+1} = \sqrt{\boldsymbol{Y}_{n+1}^D : \boldsymbol{Y}_{n+1}^{D,T}} - R = 0, \tag{42}$$

$$R_{\gamma,n+1} = \gamma_{n+1} = 0, \tag{43}$$

needs to be solved, where the last equation is simply the enforcement of the parameter γ_{n+1} to 0. For the saturated state, Eqs. (41) and (42) remain the same, while Eq. (43) is replaced with

$$R_{\gamma,n+1} = ||\boldsymbol{E}_{t,n+1}|| - \varepsilon_L = 0. \tag{44}$$

This set of equations is labelled hereinafter as PT2. Let us write PT1 and PT2 in a more compact form as:

$$\boldsymbol{Q}_{n+1} = \left\{ R_{\boldsymbol{C}_t,n+1,11}, R_{\boldsymbol{C}_t,n+1,22}, R_{\boldsymbol{C}_t,n+1,33}, R_{\boldsymbol{C}_t,n+1,12}, R_{\boldsymbol{C}_t,n+1,13}, R_{\boldsymbol{C}_t,n+1,23}, R_{\zeta,n+1}, R_{\gamma,n+1} \right\}, \tag{45}$$

and the vector of unknowns as

$$\boldsymbol{h}_{n+1} = \left\{ C_{t,n+1,11}^{-1}, C_{t,n+1,22}^{-1}, C_{t,n+1,33}^{-1}, C_{t,n+1,12}^{-1}, C_{t,n+1,13}^{-1}, C_{t,n+1,23}^{-1}, \zeta_{n+1}, \gamma_{n+1} \right\}. \tag{46}$$

The local Newton-Raphson method (with (k) denoting an iteration) is used to solve PT1 and PT2 as:

$$\left(\frac{\partial \boldsymbol{Q}_{n+1}}{\boldsymbol{h}_{n+1}} \right)^{(k)} \Delta \boldsymbol{h}_{n+1}^{(k)} = -\boldsymbol{Q}_{n+1}^{(k)}, \tag{47}$$

with the update

$$\boldsymbol{h}_{n+1}^{(k+1)} = \boldsymbol{h}_{n+1}^{(k)} + \Delta \boldsymbol{h}_{n+1}^{(k)}, \tag{48}$$

and repeated iterations until the convergence $||\Delta \boldsymbol{h}_{n+1}^{(k)}|| < tol$ is reached, with $tol = 10^{-8}$ for the numerical examples presented below.

The PT1 system (41)-(43) handles the transitions between the elastic and transformation steps, which are nucleation (i.e., $||\boldsymbol{E}_{t,n}|| = 0$ and $||\boldsymbol{E}_{t,n+1}|| > 0$) and completion (i.e., $||\boldsymbol{E}_{t,n}|| > 0$ and $||\boldsymbol{E}_{t,n+1}|| = 0$). For these steps, the tensor $\boldsymbol{N}$ is defined as given in Eq. (38), in accordance with the proposal in [36]. Therefore, $\boldsymbol{N}_{n+1}$ and $\boldsymbol{Y}_{n+1}^D$ are computed as:

$$\boldsymbol{N}_{n+1} = \frac{\dot{\boldsymbol{E}}_{t,n+1}}{||\dot{\boldsymbol{E}}_{t,n+1}||} = \frac{(\boldsymbol{C}_{n+1}^{(i)} \boldsymbol{S}_{el,n+1})^D}{||(\boldsymbol{C}_{n+1}^{(i)} \boldsymbol{S}_{el,n+1})^D||}, \tag{49}$$

$$\begin{aligned}
\boldsymbol{Y}_{n+1}^D &= (\boldsymbol{C}_{n+1}^{(i)} \boldsymbol{S}_{el,n+1} - \tau_M \boldsymbol{N}_{n+1})^D \\
&= (\boldsymbol{C}_{n+1}^{(i)} \boldsymbol{S}_{el,n+1})^D - \tau_M \underbrace{\frac{(\boldsymbol{C}_{n+1}^{(i)} \boldsymbol{S}_{el,n+1})^D}{\sqrt{(\boldsymbol{C}_{n+1}^{(i)} \boldsymbol{S}_{el,n+1})^D : (\boldsymbol{C}^{(i)} \boldsymbol{S}_{el,n+1})^D}}}_{B_{n+1}} = (\boldsymbol{C}_{n+1}^{(i)} \boldsymbol{S}_{el,n+1})^D \underbrace{\left(1 - \frac{\tau_M}{B_{n+1}} \right)}_{k_\tau}.
\end{aligned} \tag{50}$$

The trial value f^{tr} of the transformation function (35), which is computed with Eq. (50), the primal feasibility Kuhn-Tucker condition, and $k_\tau > 0$ give the following nucleation condition (NC):

$$\begin{aligned}
f^{tr} &= \sqrt{\boldsymbol{Y}_{n+1}^D : \left(\boldsymbol{Y}_{n+1}^D \right)^T} - R = k_\tau B_{n+1} - R \\
&= B_{n+1} - \tau_M - R \leq 0 \Rightarrow B_{n+1} \leq \tau_M + R.
\end{aligned} \tag{51}$$

When the condition (51) is violated, the transition from the elastic to the transformation state takes place in the current step. Similarly, with $k_\tau < 0$, the completion condition (CC) is obtained:

$$\begin{aligned}
f^{tr} &= \sqrt{\boldsymbol{Y}_{el,n+1}^D : \left(\boldsymbol{Y}_{el,n+1}^D \right)^T} - R = -k_\tau B_{n+1} - R \\
&= -B_{n+1} + \tau_M - R \leq 0 \Rightarrow B_{n+1} \leq \tau_M - R.
\end{aligned} \tag{52}$$

When the condition (52) is conformed, the transition from the transformation to the elastic state takes place. We note that the left-hand side of the final equations in (51) and (52) is always positive, as is the right-hand side of the NC in the inequality (51). However, the right-hand side of the CC in Eq. (52) can be negative for $\tau < R$, which, however, only occurs when not dealing with a superelastic regime.
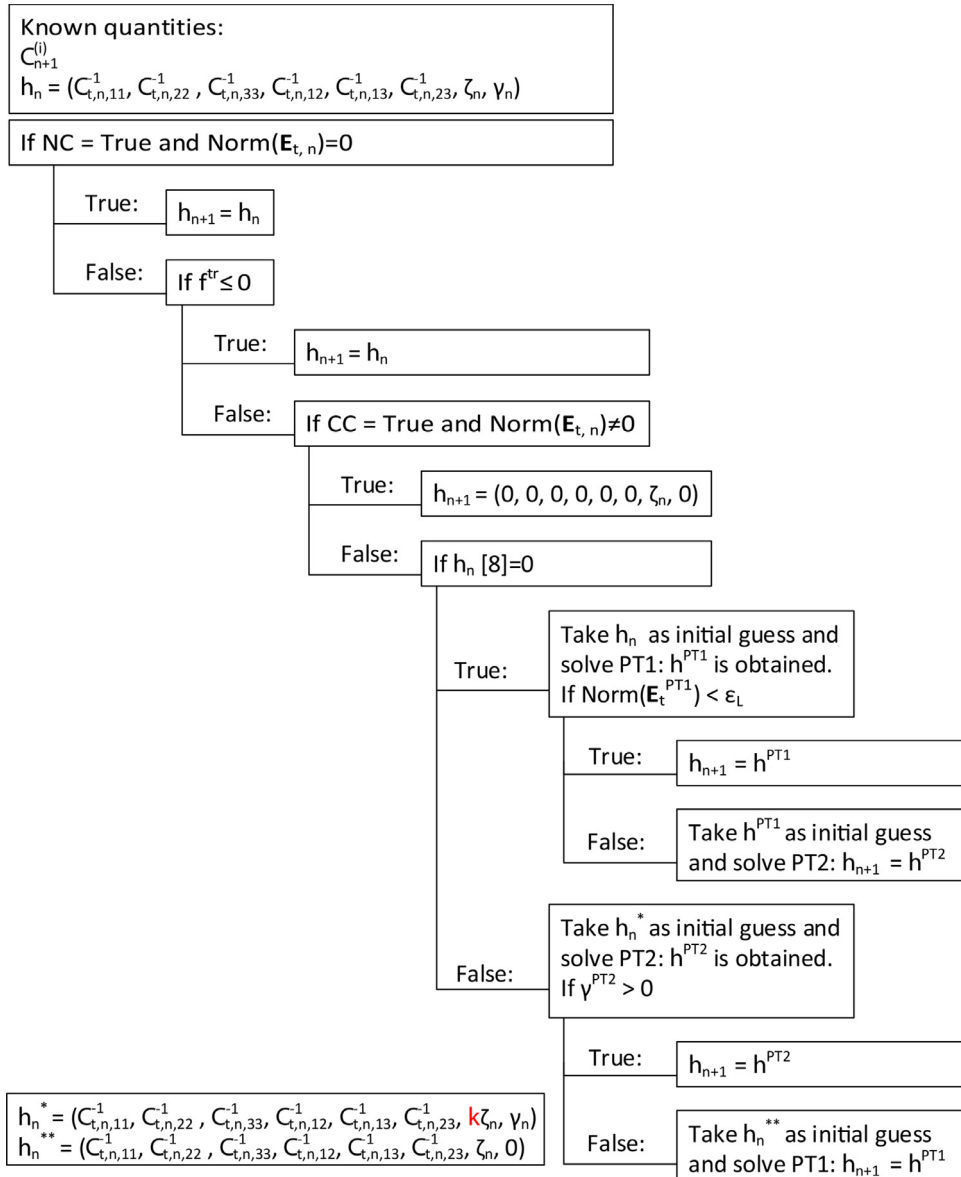
Fig. 3. Algorithm for solving local systems at the Gauss point.

2.2.2. Solving nonlinear systems at the Gauss point

It is suggested in [36] that PT1 is always solved first for an inelastic step. If the PT1 solution, labelled as $\boldsymbol{h}_{n+1}^{\mathrm{PT1}}$, is inadmissible because of the violation of condition (12), it is suggested to proceed by PT2 and compute $\boldsymbol{h}_{n+1}^{\mathrm{PT2}}$ with $\boldsymbol{h}_{n+1}^{\mathrm{PT1}}$ as the initial guess. It is our experience, however, that this procedure does not always work well.

Our numerical experiments show that much better convergence properties are obtained for the inelastic step using the algorithm presented in Fig. 3. It has four options: (i) For $\gamma_n = 0$, PT1 is solved first (with $\boldsymbol{h}_n$ as the initial guess). (ii) If the PT1 solution violates the condition (12), i.e., if $||\boldsymbol{E}_{t,n+1}|| > \varepsilon_L$ is computed, it proceeds with PT2 and takes $\boldsymbol{h}_{n+1}^{\mathrm{PT1}}$ as the initial guess. (iii) For $\gamma_n > 0$, PT2 is solved first, however, the 7th component of the initial guess $\boldsymbol{h}_n$, i.e., ζ_n, is multiplied by a factor k. Our numerical tests suggest that $k = 2$ is an effective choice. (iv) If the PT2 solution violates the condition (20), i.e., if it computes $\gamma_{n+1} < 0$, we proceed with PT1 and the modified initial guess $\boldsymbol{h}_n$ that enforces $\gamma_n = 0$.

Implementation of the line-search method, which prevents too large increments $\Delta\boldsymbol{h}^{(k)}$ in Eq. (47), also improves considerably the convergence properties. The line search introduces the parameter α_{LS} that controls the size of the increment as:

$$\boldsymbol{h}_{n+1}^{(k+1)} = \boldsymbol{h}_{n+1}^{(k)} + \alpha_{LS}\,\Delta\boldsymbol{h}_{n+1}^{(k)}, \tag{53}$$

where $0 < \alpha_{LS} \leq 1$. Usually, see [41,71], $\alpha_{LS}^{(1)} = 1$ at the beginning of each iteration. If the inequality

$$||\boldsymbol{Q}_{n+1}^{(k+1)}|| > ||\boldsymbol{Q}_{n+1}^{(k)}|| \tag{54}$$

is computed, α_{LS} is reduced by a factor $0 < \beta < 1$ (usually $\beta = 0.5$) as $\alpha_{LS}^{(j+1)} = \beta \alpha_{LS}^{(j)}$, where (j) indicates iterations of the line search loop. The loop iterates as long as the condition (54) holds. By lowering the norm of $\boldsymbol{Q}_{n+1}$, the convergence is improved in each iteration of the local Newton-Raphson loop, which, however, might require a large number of iterations. For the saturated state, the largest contribution to $||\Delta \boldsymbol{h}_{n+1}^{(k)}||$ is the change of the parameter γ. Therefore, it seems reasonable at first glance to define α_{LS} with respect to the increment $\Delta\gamma$. However, $\gamma \to \infty$ during loading (and $\gamma \to 0$ at unloading) makes the limitation of $||\Delta \boldsymbol{h}_{n+1}^{(k)}||$ troublesome. A better alternative is to define a limit value for the Lagrange multiplier $\zeta > 0$ and relate it with α_{LS} as

$$\alpha_{LS} = \begin{cases} \frac{\zeta_{limit}}{\zeta} < 1 & \text{if} \quad \zeta > \zeta_{limit} \\ 1 & \text{if} \quad \zeta \leq \zeta_{limit} \end{cases}. \tag{55}$$

The choice (55) does not guarantee descending in each local Newton-Raphson iteration because the inequality (54) might still hold in some cases; however, exceeding is small. Such a line-search procedure brings three major advantages. (i) The line-search iteration loop with α_{LS} updating is omitted. Because α_{LS} is calculated only once (if necessary) the convergence is faster. (ii) the evaluation of the inequality (54) is skipped. (iii) The allowed exceeding prevents increments that are too small $||\Delta \boldsymbol{h}_{n+1}^{(k)}||$.

3. Seven-parameter shell model and finite-element formulations

We briefly present a 7-p finite-rotation-shell model. For more details we refer to, e.g., [62,72–74]. The extensible-director kinematic hypothesis is assumed, along with the quadratic through-the-thickness variation of displacements. We adopt the standard notation for the indices: small Greek letters for indices from $1, 2$ and small Latin letters for indices from $1, 2, 3$.

3.1. 7-p shell model

The shell is embedded in 3D space with a fixed orthonormal basis $\{\boldsymbol{e}_i\}$. It is described as a surface with an extensible-director field, with the position vector to the material point in the initial configuration given as:

$$\boldsymbol{X}\left(\xi^1, \xi^2, \xi^3\right) = \boldsymbol{\varphi}_0\left(\xi^1, \xi^2\right) + \xi^3 \boldsymbol{D}\left(\xi^1, \xi^2\right), \quad \xi^3 \in [-h/2, h/2], \quad \left(\xi^1, \xi^2\right) \in \mathcal{A}, \quad ||\boldsymbol{D}|| = 1, \tag{56}$$

where ξ^i are the convected curvilinear coordinates. Hereinafter, we will omit writing the functions' and functionals' arguments for brevity. Thus, $\boldsymbol{\varphi}_0$ describes the shell mid-surface $\mathcal{M}$, $\boldsymbol{D}$ is the normal-to-the-$\mathcal{M}$ vector field of unit length that is called the shell director, h is the initial shell thickness, and $\mathcal{A}$ is the domain for the mid-surface parametrization. The position vector to the material point in the deformed (current) configuration is assumed to be:

$$\boldsymbol{x} = \underbrace{\boldsymbol{\varphi}_0 + \boldsymbol{u}}_{\boldsymbol{\varphi}} + \xi^3 \underbrace{\overline{\lambda} \boldsymbol{a}}_{\boldsymbol{d}} + \left(\xi^3\right)^2 \underbrace{q \boldsymbol{a}}_{\boldsymbol{f}}, \quad ||\boldsymbol{a}|| = 1, \tag{57}$$

where $\boldsymbol{u}$ is the mid-surface displacement vector field, $\overline{\lambda}$ is the scalar through-the-thickness-stretching field, and q is the hierarchical scalar field related with the quadratic variation of displacements in the through-the-thickness direction. Moreover, $\boldsymbol{a}$ is the rotated shell director field in the deformed configuration, see, e.g., [75–77] for details. With (56) and (57), the covariant base vectors for the initial and deformed configurations are

$$\boldsymbol{G}_\alpha = \frac{\partial \boldsymbol{X}}{\partial \xi^\alpha} = \boldsymbol{\varphi}_{0,\alpha} + \xi^3 \boldsymbol{D}_{,\alpha}, \quad \boldsymbol{G}_3 = \frac{\partial \boldsymbol{X}}{\partial \xi^3} = \boldsymbol{D},$$

$$\boldsymbol{g}_\alpha = \frac{\partial \boldsymbol{x}}{\partial \xi^\alpha} = \boldsymbol{\varphi}_{,\alpha} + \xi^3 \boldsymbol{d}_{,\alpha} + \left(\xi^3\right)^2 \boldsymbol{f}_{,\alpha}, \quad \boldsymbol{g}_3 = \frac{\partial \boldsymbol{x}}{\partial \xi^3} = \boldsymbol{d} + 2\xi^3 \boldsymbol{f}, \tag{58}$$

where $\boldsymbol{d}_{,\alpha} = \overline{\lambda}_{,\alpha} \boldsymbol{a} + \overline{\lambda} \boldsymbol{a}_{,\alpha}$ and $\boldsymbol{f}_{,\alpha} = q_{,\alpha} \boldsymbol{a} + q \boldsymbol{a}_{,\alpha}$. The dual base vectors $\boldsymbol{G}^i$ are defined through the orthogonal condition $\boldsymbol{G}^i \cdot \boldsymbol{G}_j = \delta_j^i$, where δ_j^i is the Kronecker delta symbol. The Green-Lagrange strain tensor for the considered shell model is defined as:

$$\check{\boldsymbol{E}} = \frac{1}{2}\left(\boldsymbol{g}_i \cdot \boldsymbol{g}_j - \boldsymbol{G}_i \cdot \boldsymbol{G}_j\right) \boldsymbol{G}^i \otimes \boldsymbol{G}^j = \check{E}_{ij} \boldsymbol{G}^i \otimes \boldsymbol{G}^j, \tag{59}$$

with the covariant components of the strain tensor given as functions of ξ^3, see [73]:

$$\check{E}_{ij} = H_{ij} + \xi^3 K_{ij} + \left(\xi^3\right)^2 L_{ij} + \left(\xi^3\right)^3 M_{ij} + \left(\xi^3\right)^4 N_{ij}. \tag{60}$$

Following [73], we truncate (60) after the quadratic term, thus introducing the reduction

$$\check{E}_{ij} \to E_{ij} = H_{ij} + \xi^3 K_{ij} + \left(\xi^3\right)^2 L_{ij}. \tag{61}$$

The explicit forms of the covariant components of the reduced strain tensor $\boldsymbol{E} = E_{ij}\boldsymbol{G}^i \otimes \boldsymbol{G}^j$ are:

$$H_{\alpha\beta} = \frac{1}{2}\left(\boldsymbol{\varphi}_{,\alpha} \cdot \boldsymbol{\varphi}_{,\beta} - \boldsymbol{\varphi}_{0,\alpha} \cdot \boldsymbol{\varphi}_{0,\beta}\right), \quad H_{\alpha 3} = \frac{1}{2}(\boldsymbol{\varphi}_{,\alpha} \cdot \mathrm{d} - \underbrace{\boldsymbol{\varphi}_{0,\alpha} \cdot \boldsymbol{D}}_{0}), \quad H_{33} = \frac{1}{2}(\boldsymbol{d} \cdot \boldsymbol{d} - \boldsymbol{D} \cdot \boldsymbol{D}) = \frac{1}{2}\left(\overline{\lambda}^2 - 1\right), \tag{62}$$

$$K_{\alpha\beta} = \frac{1}{2}\left(\boldsymbol{\varphi}_{,\alpha} \cdot \boldsymbol{d}_{,\beta} + \boldsymbol{\varphi}_{,\beta} \cdot \boldsymbol{d}_{,\alpha} - \boldsymbol{\varphi}_{0,\alpha} \cdot \boldsymbol{D}_{,\beta} - \boldsymbol{\varphi}_{0,\beta} \cdot \boldsymbol{D}_{,\alpha}\right),$$

$$K_{\alpha 3} = \frac{1}{2}(\boldsymbol{d}_{,\alpha} \cdot \boldsymbol{d} + 2\boldsymbol{\varphi}_{,\alpha} \cdot \boldsymbol{f} - \underbrace{\boldsymbol{D}_{,\alpha} \cdot \boldsymbol{D}}_{0}), \quad K_{33} = \frac{1}{2}(4\boldsymbol{f} \cdot \boldsymbol{d}) = 2\boldsymbol{f} \cdot \boldsymbol{d} = 2q\overline{\lambda}, \tag{63}$$

$$L_{\alpha\beta} = \frac{1}{2}\left(\boldsymbol{d}_{,\alpha} \cdot \boldsymbol{d}_{,\beta} + \boldsymbol{\varphi}_{,\alpha} \cdot \boldsymbol{f}_{,\beta} + \boldsymbol{\varphi}_{,\beta} \cdot \boldsymbol{f}_{,\alpha} - \boldsymbol{D}_{,\alpha} \cdot \boldsymbol{D}_{,\beta}\right),$$

$$L_{\alpha 3} = \frac{1}{2}\left(2\boldsymbol{d}_{,\alpha} \cdot \boldsymbol{f} + \boldsymbol{f}_{,\alpha} \cdot \boldsymbol{d}\right), \quad L_{33} = \frac{1}{2}(4\boldsymbol{f} \cdot \boldsymbol{f}) = 2\boldsymbol{f} \cdot \boldsymbol{f} = 2q^2. \tag{64}$$

We note that in the computer code the covariant components (62)–(64) are transformed to the Cartesian components using the local Cartesian basis defined for each integration point.

The weak form of the equilibrium equations at time t_{n+1} is (index $n + 1$ is omitted hereinafter for brevity):

$$G(\Phi, \boldsymbol{C}_t, \delta\Phi) = \int_{\mathscr{M}} \int_{-h/2}^{h/2} \delta\boldsymbol{E}(\Phi, \delta\Phi) : \boldsymbol{S}(\boldsymbol{E}(\Phi), \boldsymbol{C}_t)dV - G_{ext}(\delta\Phi) = 0, \tag{65}$$

where $\Phi = \{\boldsymbol{u}, \boldsymbol{a}, \overline{\lambda}, q\}$ is the set of unknown functions called generalized displacements, $\delta\Phi = \left[\delta\boldsymbol{u}, \delta\boldsymbol{a}, \delta\overline{\lambda}, \delta q\right]^{\mathrm{T}}$ is the vector of admissible variations of Φ, and $\delta\boldsymbol{E} = \partial\boldsymbol{E}/\partial\Phi \cdot \delta\Phi = \frac{d}{d\epsilon}[\boldsymbol{E}(\Phi + \epsilon\delta\Phi)]_{\epsilon=0}$ is the variation of the reduced strain tensor.

After the spatial discretization of the mid-surface $\mathscr{M}$ with n_{el} non-overlapping finite elements, such that $\mathscr{M} \approx \bigcup_{e=1}^{n_{el}} A_e$, and after using the appropriate interpolation for generalized displacements and their admissible variations, the functional (65) becomes an assembly of the finite-element contributions, with the mesh-related nodal values for generalized displacements and the Gauss-point-related values for the transformation tensor $\boldsymbol{C}_t$ as the unknowns:

$$G = \mathbb{A}_{e=1}^{n_{el}} \left(\underbrace{G_{int}^e(\Phi^e, \boldsymbol{C}_t, \delta\Phi^e) - G_{ext}^e\left(\delta\Phi^e\right)}_{=0} \right) = 0. \tag{66}$$

Here, $\mathbb{A}$ denotes the finite-element-assembly operator, e.g., [67], and G_{int}^e and G_{ext}^e denote the element's approximation of the first and second terms on the right-hand side of Eq. (65), respectively:

$$G^e = \int_{A_e} \int_{-h/2}^{h/2} \delta\boldsymbol{E}(\Phi^e, \delta\Phi^e) : \boldsymbol{S}(\boldsymbol{E}(\Phi^e), \boldsymbol{C}_t)dV - G_{ext}^e\left(\delta\Phi^e\right) = 0. \tag{67}$$

The current values of the stress tensor are obtained using the algorithm presented in Section 2.2, which is one of the two steps of the operator-split method. For the other step, where the solution $\mathbb{A}_{e=1}^{n_{el}} \Phi^e$ is computed for a given loading, the linearization of (67) is needed, which can be written as $\mathrm{Lin}(G^e) = G^e + \Delta G^e$, where

$$\Delta G^e = \int_{A_e} \int_{-h/2}^{h/2} (\delta\boldsymbol{E} : \mathbb{C} \ \Delta\boldsymbol{E} + \Delta(\delta\boldsymbol{E}) : \boldsymbol{S})dV. \tag{68}$$

Here, $\mathbb{C} = \partial\boldsymbol{S}/\partial\boldsymbol{E}$ is the fourth-order tensor, called the consistent inelastic tangent operator, which is computed already in the first step, and

$$\Delta\boldsymbol{E} = \frac{\partial\boldsymbol{E}}{\partial\Phi^e} \cdot \Delta\Phi^e, \quad \delta\boldsymbol{E} = \frac{\partial\boldsymbol{E}}{\partial\Phi^e} \cdot \delta\Phi^e, \quad \Delta(\delta\boldsymbol{E}) = \frac{\partial(\delta\boldsymbol{E})}{\partial\Phi^e} \cdot \Delta\Phi^e. \tag{69}$$

3.2. Three 7-p quadrilateral finite-element formulations

We describe the assumed natural strain (ANS) and the enhanced assumed strain (EAS) interpolations that are applied for three 7-p quadrilateral finite elements used to compute the numerical examples.

3.2.1. Basic interpolations

The initial mid-surface and the initial shell director over the quadrilateral 7-p shell finite element are interpolated as

$$\boldsymbol{\varphi}_0^e = \sum_{a=1}^{4} N_a(\xi, \eta)\boldsymbol{\varphi}_{0a}, \quad \boldsymbol{D}^e = \sum_{a=1}^{4} N_a(\xi, \eta)\boldsymbol{D}_a, \quad \|\boldsymbol{D}_a\| = 1, \tag{70}$$
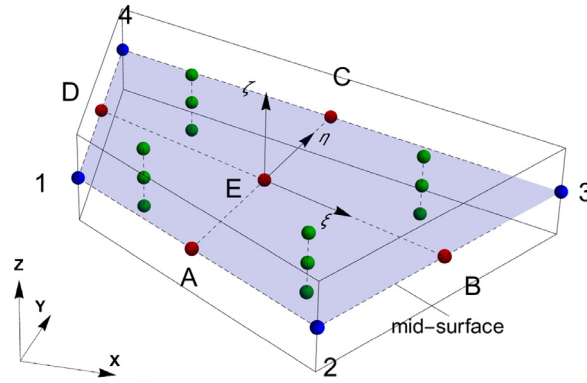
Fig. 4. 7-p shell quadrilateral finite element with ANS points.

where $(\cdot)_a$ are the nodal values, $\boldsymbol{D}_a$ is the exact normal to the shell mid-surface at node a, and $\xi \in [-1, \ 1]$ and $\eta \in [-1, \ 1]$ are the isoparametric coordinates that parametrize element's mid-surface and approximate ξ^1 and ξ^2 over A_e. Moreover, $N_a(\xi, \eta)$ are bilinear Lagrange interpolation functions defined over the bi-unit square $[-1, \ 1] \times [-1, \ 1]$. In order to have zero values of all the kinematic variables for the initial configuration, we introduce an auxiliary kinematic variable $\widetilde{\lambda}$ as

$$\widetilde{\lambda} = 1 - \overline{\lambda}. \tag{71}$$

The deformed configuration of the element is approximated with:

$$\boldsymbol{u}^e(\xi, \eta) = \sum_{a=1}^{n_{en}} N_a(\xi, \eta) \boldsymbol{u}_a, \quad \boldsymbol{a}^e = \sum_{a=1}^{n_{en}} N_a(\xi, \eta) \boldsymbol{a}_a, \tag{72}$$

$$\widetilde{\lambda}^e = \sum_{a=1}^{4} N_a(\xi, \eta) \widetilde{\lambda}_a, \quad q^e = \sum_{a=1}^{4} N_a(\xi, \eta) q_a. \tag{73}$$

Note that the interpolations for the shell director (71) and (72) demand applying the rotations and rotational parameters only at the nodes of the finite element.

3.2.2. ANS enhancements

To avoid the transverse shear, the membrane, and the through-the-thickness lockings, and to reduce the sensitivity of the quadrilateral shell element to geometric distortion, the ANS interpolations are used.

For the membrane covariant components of the strain tensor, we adopt the ANS interpolation proposed by Kulikov and Plotnikova [63] for the five-parameter (5-p) quadrilateral shell element:

$$E_{11}^{ANS} = \left(-1 + \eta^2\right) \left(a_B E_{11}^B + a_D E_{11}^D + a_E E_{12}^E\right) + \frac{1}{2} \left(1 - 2a_A - \eta + 2a_A \eta^2\right) E_{11}^A + \frac{1}{2} \left(1 - 2a_C + \eta + 2a_C \eta^2\right) E_{11}^C, \tag{74}$$

$$E_{22}^{ANS} = \left(-1 + \xi^2\right) \left(a_A E_{22}^A + a_C E_{22}^C + a_E E_{12}^E\right) + \frac{1}{2} \left(1 - 2a_B + \xi + 2a_B \xi^2\right) E_{22}^B + \frac{1}{2} \left(1 - 2a_D - \xi + 2a_D \xi^2\right) E_{22}^D, \tag{75}$$

$$
\begin{aligned}
E_{12}^{ANS} &= \tfrac{1}{4} \left(-\xi + 4a_A \xi \eta\right) E_{11}^A + \tfrac{1}{4} \left(\xi + 4a_C \xi \eta\right) E_{11}^C + \tfrac{1}{4} \left(\eta + 4a_B \xi \eta\right) E_{22}^B + \\
&\quad + \tfrac{1}{4} \left(-\eta + 4a_D \xi \eta\right) E_{22}^D + \left(1 + a_E \xi \eta\right) E_{12}^E,
\end{aligned} \tag{76}
$$

where A, B, C, D and E define the points where the strains are evaluated with Eqs. (61)–(64), see Fig. 4. The a factors that appear in the above expressions measure the mesh distortion, e.g. [63–66]. For our element called 3ANS, they were computed for the last converged configuration [65], and for our element called EAS, they were computed for the initial configuration.

For the transverse shear covariant components of the strain tensor, we adopt the ANS interpolation proposed by Dvorkin and Bathe [61] for the quadrilateral based on the 5-p shell model:

$$E_{13}^{ANS} = \frac{1}{2} \left((1-\eta) E_{13}^A + (1+\eta) E_{13}^C\right), \quad E_{23}^{ANS} = \frac{1}{2} \left((1-\xi) E_{23}^D + (1+\xi) E_{23}^B\right). \tag{77}$$

Equations (61)–(64) are used to compute the transverse shear strains at the collocation points A, B, C and D, see Fig. 4. Finally, for the transverse normal covariant component of the strain tensor, we adopt the ANS interpolation proposed by Betsch and Stein [62]:

$$E_{13}^{ANS} = \sum_{a=1}^{4} N_a(\xi, \eta) E_{33a}. \tag{78}$$

Table 1
Used finite elements.

FE	$H_{\alpha\beta}$	$H_{\alpha 3}$	H_{33}	$K_{\alpha\beta}$	$K_{\alpha 3}$	K_{33}	$L_{\alpha\beta}$	$L_{\alpha 3}$	L_{33}
2ANS	Disp.	ANS	ANS	Disp.	ANS	ANS	Disp.	ANS	ANS
3ANS	ANS	ANS	ANS	ANS	ANS	ANS	ANS	ANS	ANS
EAS	ANS & EAS (5)	ANS	ANS & EAS (3)	ANS & EAS (5)	ANS	ANS & EAS (3)	ANS & EAS (5)	ANS	ANS

By using the above ANS enhancements, the strain tensor changes as $\boldsymbol{E} \to \boldsymbol{E}^{ANS}$, which is reflected in the element's weak form (67) simply by the replacement of $\boldsymbol{E}$ with $\boldsymbol{E}^{ANS}$.

3.2.3. EAS enhancements

The performance of the element can also be improved by application of the EAS concept, which relies on the enhancement of the covariant components of the strain tensor by adding the enhancing components. The in-plane covariant components of the strain tensor, $H_{\alpha\beta}$, $K_{\alpha\beta}$ and $L_{\alpha\beta}$, can be additively enhanced by covariant components of the enhancing strain tensor denoted as $\tilde{H}_{\alpha\beta}$, $\tilde{K}_{\alpha\beta}$ and $\tilde{L}_{\alpha\beta}$. The latter can be collected in vectors as

$$\widetilde{\boldsymbol{H}}_{\alpha\beta} = \left[\tilde{H}_{11}, \tilde{H}_{22}, 2\tilde{H}_{12}\right]^T, \quad \widetilde{\boldsymbol{K}}_{\alpha\beta} = \left[\tilde{K}_{11}, \tilde{K}_{22}, 2\tilde{K}_{12}\right]^T, \qquad \widetilde{\boldsymbol{L}}_{\alpha\beta} = \left[\tilde{L}_{11}, \tilde{L}_{22}, 2\tilde{L}_{12}\right]^T, \tag{79}$$

and interpolated over the element as

$$\widetilde{\boldsymbol{H}}_{\alpha\beta} = \boldsymbol{\Gamma}^{IP}\widetilde{\boldsymbol{\alpha}}_{H_{\alpha\beta}}, \quad \widetilde{\boldsymbol{K}}_{\alpha\beta} = \boldsymbol{\Gamma}^{IP}\widetilde{\boldsymbol{\alpha}}_{K_{\alpha\beta}}, \quad \widetilde{\boldsymbol{L}}_{\alpha\beta} = \boldsymbol{\Gamma}^{IP}\widetilde{\boldsymbol{\alpha}}_{L_{\alpha\beta}}, \tag{80}$$

where the interpolation was chosen based on experience with 5-p shell quadrilaterals, e.g., [65,66,78], as

$$\boldsymbol{\Gamma}^{IP} = \begin{bmatrix} \xi & 0 & 0 & 0 & 0 \\ 0 & \eta & 0 & 0 & 0 \\ 0 & 0 & \xi & \eta & \xi\eta \end{bmatrix}. \tag{81}$$

In (80), $\widetilde{\boldsymbol{\alpha}}_{H_{\alpha\beta}}$, $\widetilde{\boldsymbol{\alpha}}_{K_{\alpha\beta}}$ and $\widetilde{\boldsymbol{\alpha}}_{L_{\alpha\beta}}$ are vectors of the additional EAS parameters of the element, with each vector having five parameters. The EAS enhancement of the in-plane covariant strains can therefore be written as $\widetilde{\boldsymbol{E}}_{\alpha\beta} = \widetilde{\boldsymbol{H}}_{\alpha\beta} + \xi^3\widetilde{\boldsymbol{K}}_{\alpha\beta} + \left(\xi^3\right)^2\widetilde{\boldsymbol{L}}_{\alpha\beta}$. Also, the through-the-thickness normal covariant components of the strain tensor, H_{33} and K_{33}, can be additively enhanced by the EAS strains. We use the following interpolations

$$\tilde{H}_{33} = \boldsymbol{\Gamma}^{TH}\widetilde{\boldsymbol{\alpha}}_{H_{33}}, \quad \widetilde{K}_{33} = \frac{j_C}{j_G}\boldsymbol{\Gamma}^{TH}\widetilde{\boldsymbol{\alpha}}_{K_{33}}, \tag{82}$$

where

$$\boldsymbol{\Gamma}^{TH} = \begin{bmatrix} \xi & \eta & \xi\eta \end{bmatrix}, \tag{83}$$

and the vectors $\widetilde{\boldsymbol{\alpha}}_{H_{33}}$ and $\widetilde{\boldsymbol{\alpha}}_{K_{33}}$ consist of three additional EAS parameters each. We note that in the computations, the components of the strain and stress tensors with respect to the local Cartesian basis are used in the Gauss points. The transformation of the covariant generalized-displacement-based, ANS, and EAS strain components is performed in the standard manner, see, e.g., [66].

The variational framework for the EAS enhancements is a modified Hu-Washizu functional, which is without the stress tensor (e.g., [78,79]), and with the strain tensor defined as $\boldsymbol{E}^{EAS} = \boldsymbol{E} + \widetilde{\boldsymbol{E}}$. Its stationary point provides two equations:

$$G^{e,EAS,1} = \int_{A_e} \int_{-h/2}^{h/2} \delta\boldsymbol{E}(\Phi^e, \delta\Phi^e) : \frac{\partial\tilde{\psi}}{\partial\boldsymbol{E}^{EAS}}\left(\boldsymbol{E}(\Phi^e) + \widetilde{\boldsymbol{E}}, \boldsymbol{C}_t\right)dV - G^e_{ext}\left(\delta\Phi^e\right) = 0, \tag{84}$$

$$G^{e,EAS,2} = \int_{A_e} \int_{-h/2}^{h/2} \delta\widetilde{\boldsymbol{E}} : \frac{\partial\tilde{\psi}}{\partial\boldsymbol{E}^{EAS}}\left(\boldsymbol{E}(\Phi^e) + \widetilde{\boldsymbol{E}}, \boldsymbol{C}_t\right)dV = 0, \tag{85}$$

among which (85) is used for condensation of the additional EAS parameters at the element level. As shown for the 5-p shell model quadrilateral [65,80,81], combining the ANS and EAS concepts as $\boldsymbol{E}^{EAS*} = \boldsymbol{E}^{ANS} + \widetilde{\boldsymbol{E}}$ leads to very efficient formulations. In that case, (84) and (85) change to

$$G^{e,\ EAS*,1} = \int_{A_e} \int_{-h/2}^{h/2} \delta\boldsymbol{E}^{ANS}(\Phi^e, \delta\Phi^e) : \frac{\partial\tilde{\psi}}{\partial\boldsymbol{E}^{EAS*}}\left(\boldsymbol{E}^{ANS}(\Phi^e) + \widetilde{\boldsymbol{E}},\ \boldsymbol{C}_t\right)dV - G^e_{ext}\left(\delta\Phi^e\right) = 0, \tag{86}$$

$$G^{e,EAS*,2} = \int_{A_e} \int_{-h/2}^{h/2} \delta\widetilde{\boldsymbol{E}} : \frac{\partial\tilde{\psi}}{\partial\boldsymbol{E}^{EAS*}}\left(\boldsymbol{E}^{ANS}(\Phi^e) + \widetilde{\boldsymbol{E}},\ \boldsymbol{C}_t\right)dV = 0. \tag{87}$$

The interpolations for the three finite elements applied in the section with numerical examples are listed in Table 1, where "Disp." stands for standard, generalized-displacement-based interpolation, and the number in parenthesis denotes the number of EAS parameters in the EAS formulations.
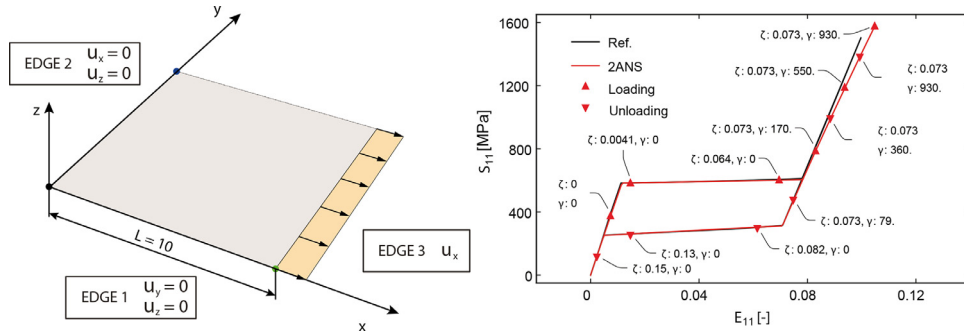
Fig. 5. Square element in tension: geometry, boundary conditions and loading (left) and superelastic response at the Gauss point (right).

4. Numerical examples

The computer codes for the above-described material and shell models were produced using the finite-element code generator AceGen, see [69,70]. They were implemented into the finite-element computer code AceFEM [82] that was used to compute the numerical examples given below. Three sets of material parameters are used: Set 1, see (88), is taken from Arghavani et al. [36], Set 2, see (89), is taken from Evangelista et al. [35], and Set 3, see (90), is calibrated to match the experiment in [83].

$$\text{Set 1:} \quad E = 51700 \,\text{MPa}, \quad \nu = 0.3, \quad \bar{h} = 750 \,\text{MPa}, \quad R = 140 \,\text{MPa},$$
$$\varepsilon_L = 0.075, \quad \beta = 5.6 \,\text{MPa/}^\circ\text{C}, \quad T_0 = -25\,^\circ\text{C}, \tag{88}$$

$$\text{Set 2:} \quad E = 53000 \,\text{MPa}, \quad \nu = 0.36, \quad \bar{h} = 1000 \,\text{MPa}, \quad R = 50 \,\text{MPa},$$
$$\varepsilon_L = 0.04, \quad \beta = 2.1 \,\text{MPa/}^\circ\text{C}, \quad T_0 = -50.15\,^\circ\text{C}, \tag{89}$$

$$\text{Set 3:} \quad E = 40000 \,\text{MPa}, \quad \nu = 0.33, \quad \bar{h} = 270 \,\text{MPa}, \quad R = 82.5 \,\text{MPa},$$
$$\varepsilon_L = 0.059, \quad \beta = 5.6 \,\text{MPa/}^\circ\text{C}, \quad T_0 = -7.8\,^\circ\text{C}. \tag{90}$$

To obtain the superelastic response, the ambient temperature T is set to 37°C for Set 1, to 11.85°C for Set 2, and to 27.5°C for Set 3. The numerical examples were computed with all three formulations (2ANS, 3ANS and EAS) using a $2 \times 2 \times 3$ Gaussian quadrature, i.e., with three integration points in the thickness direction. For examples with identical results for all formulations, the label "2ANS" is used in the figures below. Where the results are identical for the 2ANS and 3ANS, but not for the EAS, the labels "2ANS" and "EAS" are used. The components of the second Piola-Kirchhoff stress tensor and the components of the Green-Lagrange strain tensor are shown when presenting the response at the integration point.

4.1. Tension of a square element

A square element with an edge length $L = 10$ mm and a thickness $h = 0.01$ mm is subjected to tension. The supports are applied in such a way that the homogeneous stress state is obtained (see Fig. 5 (left)). The edge 3 is subjected to an imposed displacement $u_x = u_{\max} \lambda$, where $u_{\max} = 1$ mm and λ is a load multiplier. Set 1 of the material parameters is used. Loading and unloading with a total of 320 steps is considered, with λ increasing from 0 to 1 and decreasing back to 0. The stress-strain relation at the integration point is shown in Fig. 5 (right). Comparing the curve with that from Arghavani et al. [36] (labelled as "Ref."), only a small discrepancy is observed for large stresses due to the use of different strain-energy functions. Namely, we use the Neo-Hokean strain-energy function, while in [36] the Saint-Venant Kirchhoff model was applied. Moreover, the reference curve from Arghavani et al. [36] was obtained by directly solving local equations that appear at the Gauss point for the plane-stress case, while our results are obtained by applying a load to a single finite element. Characteristic points are marked on the curve to show how the variables ζ and γ are changing during loading and unloading. In the beginning, the response is elastic, therefore $\zeta = \gamma = 0$. During the forward martensitic transformation, the PT1 system is being solved and ζ is increasing. When the transformation is completed, the saturated state is present, and therefore the PT2 system gives an admissible converged solution with the constant ζ and an increasing γ. The higher the load, the greater the value for γ. At the beginning of the unloading, the first few steps are elastic, because the Kuhn-Tucker condition for the limit function is not violated ($f^{tr} < 0$). With further unloading, ζ remains constant and γ is decreasing towards 0. At the beginning of the reverse transformation, $\gamma = 0$ and the unsaturated state is present. During the reverse transformation, ζ is increasing, while γ remains at 0 and the PT1 system is being solved. After completion of the reverse transformation, the elastic response is obtained, i.e., ζ and γ are constant.
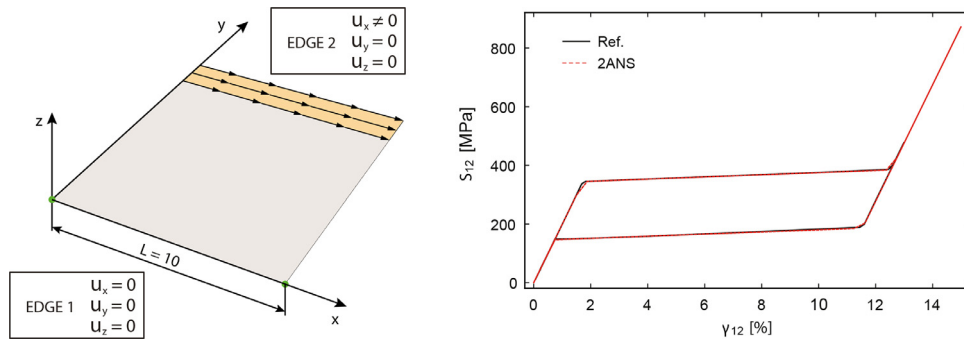
Fig. 6. Square element under shear: geometry, boundary conditions, loading (left) and superelastic response at Gauss point (right).
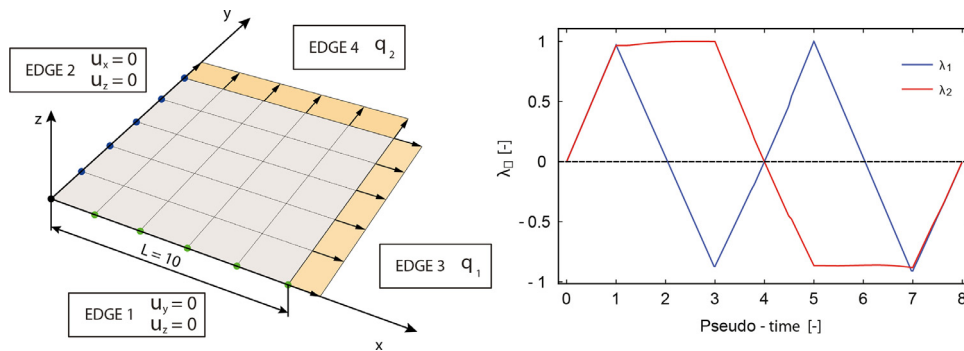

Fig. 7. Square wall: geometry, mesh, boundary conditions and loading (left) and change of multipliers (right).

4.2. Shear of a square element

A square element with the edge length $L = 10$ mm and thickness $h = 0.01$ mm is subjected to a shear load, see Fig. 6 (left). The displacement $u_x = \lambda u_{max}$ is imposed on edge 2, where $u_{max} = 1.5$ mm and λ is the load multiplier. Loading and unloading in a total of 80 steps is considered by increasing λ from 0 to 1 and decreasing it back to 0. The Set 1 of the material parameters is used. With the boundary conditions shown in Fig. 6 (left), a homogeneous stress state is obtained. We note that for a mesh of several elements, this is no more the case, because this kind of loading does not produce a pure shear state in a nonlinear neo-Hookean solid. Nevertheless, we use a single-element test in order to compare our results with the pure shear test reported in [36]. We can see from Fig. 6 (right) that our curve matches perfectly with the curve "Ref." from Arghavani et al. [36]. It is worth mentioning that the reference curve is obtained by directly solving the local equations that appear at the Gauss point for the pure-shear case, while our results are obtained by applying a load on a single finite element.

4.3. Square wall in tension and compression

A square wall with the edge length $L = 10$ mm and thickness $h = 0.01$ mm is subjected to non-proportional loading. The wall is supported along the edges 1 and 2 in such a way that a homogeneous stress state is obtained (see Fig. 7 (left)). A structured mesh of 5×5 elements is used, along with the Set 1 of material parameters.

The loads are $q_1 = \lambda_1 q_{1,max}$ and $q_2 = \lambda_2 q_{2,max}$, where λ_1 and λ_2 are the load multipliers, and $q_{1,max} = 7.524$ N/mm and $q_{2,max} = 7.559$ N/mm. The values of the load multipliers are adjusted load-step-wise, as shown in Fig. 7 (right), so that the butterfly-like stress pattern from Fig. 8 (left) is obtained, with the maximum stresses $S_{11} = S_{22} = 700$ MPa. This allows us to compare our results with those from Arghavani et al. [36] in Fig. 8 (right), where the normal in-plane strains are shown. Our results fit well with the reference results, which were obtained with the Gauss-point algorithm for the butterfly-like stress control shown in Fig. 8 (left).

4.4. Beam in tension

A straight beam of length $L = 100$ mm, width $w = 20$ mm, and thickness $h = 1$ mm is subjected on edge 2, see Fig. 9, to a tensile load $q_1 = q \lambda$, where $q = 400$ N/mm and λ is the load multiplier (after [35]). The mesh is 10×1 elements, and the Set 2 material parameters are used. The loading and unloading is considered, with λ increasing from 0 to 1 and decreasing back to 0. Four cases of boundary conditions are studied. The first three cases have the edge 1 supported as $u_x = u_y = u_z = 0$.
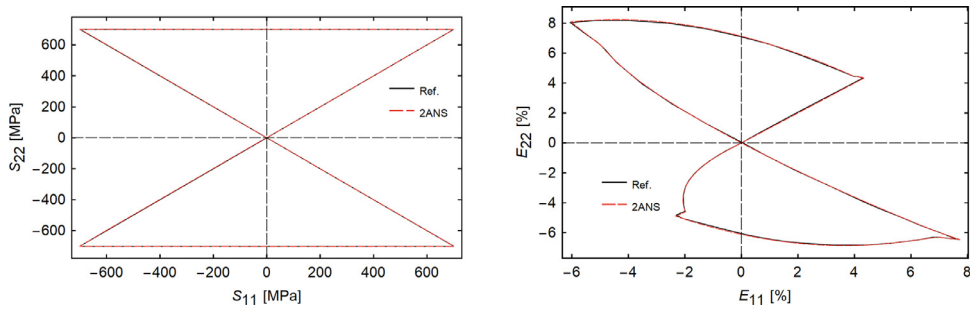
Fig. 8. Square wall: computed stress pattern (left) and superelastic response at the Gauss point (right).
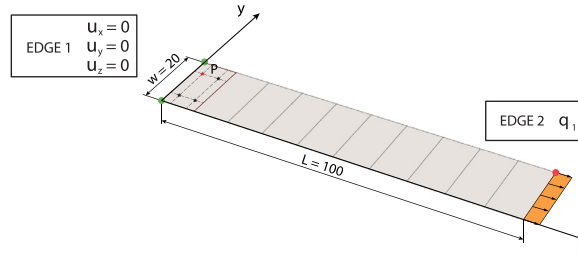

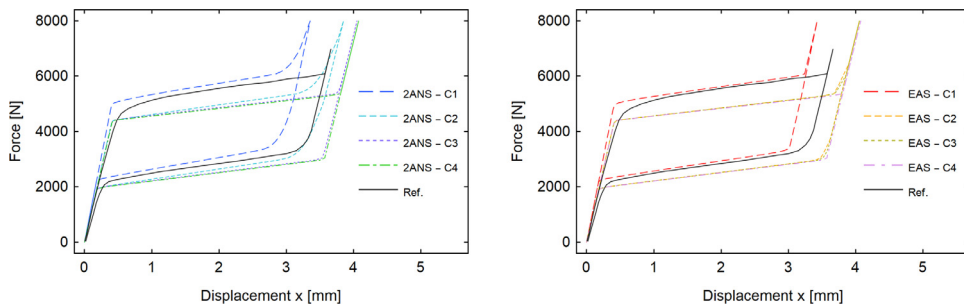**Fig. 9.** Beam in tension: geometry, mesh, loading and boundary conditions (C3).

Fig. 10. Beam in tension: superelastic response.

Additionally, for the first case (C1), the thickness change (i.e., the 6th and the 7th nodal degrees of freedom) is restricted to zero over the whole mesh. For the second case (C2), the thickness change is restricted to zero only on edge 1, while for the third case (C3), no additional boundary conditions are applied. For the fourth case (C4), the point with coordinates (0,0,0) is restrained as $u_x = u_y = u_z = 0$, and the rest of the edge 1 is restrained as $u_x = u_z = 0$ (giving a homogeneous stress state). Thus, C1 is the plane-strain case, and C3 and C4 are the plane-stress cases.

The results show that for the plane-strain case C1, $E_{33} = 0$ for 2ANS and 3ANS, and $E_{33} \approx 10^{-3}$ for EAS. For the plane-stress cases (C3 and C4), $S_{33} \approx 0$ for EAS, which, however, is not the case for 2ANS and 3ANS. For C2, the influence of the edge support is much larger for 2ANS and 3ANS than for EAS. Figure 10 shows the axial force at edge 1 versus the axial displacement of the point with initial coordinates $(L, w, 0)$. Interestingly, the difference between the computed stresses and strains for the three formulations reflects only slightly in the load-displacement curves for C1, C3 and C4, and it is considerable only for C2. The curves are compared with those of Evangelista et al. [35], who used a mesh of 10×1 2D elements that were claimed as plane stress, and C3 boundary conditions. It can be observed that none of our curves matches with that from Evangelista et al. [35]. It seems that the results from Evangelista et al. [35] are neither plane stress nor plane strain, but, unfortunately, a description of the applied 2D element and the corresponding SMA formulation are not provided in [35]. Part of the difference between our results and those of [35] can be attributed to our use of the nucleation and completion conditions, while [35] used a regularized norm for $||\boldsymbol{E}_t||$, which means that the material is treated as inelastic from the start of the analysis. This makes a sharp transition at the beginning of the transformation (when loading) and at the end of transformation (when unloading) in our formulations. Figure 11 shows distribution of non-zero stresses through the thickness of EAS element: at the near-support-point marked with P in Fig. 9, for C3, at $\lambda = 1$, and for 3, 5 and 7 through-the-thickness integration points.

Small values of S_{33} (in the range of $10^{-3} S_{11}$) and S_{13} (in the range of $10^{-2} S_{11}$) are observed, with integral of S_{13} over the thickness yielding zero. It seems that our 7-p formulations exhibit slight 3D effects (expressed by non-zero S_{33} and S_{13}
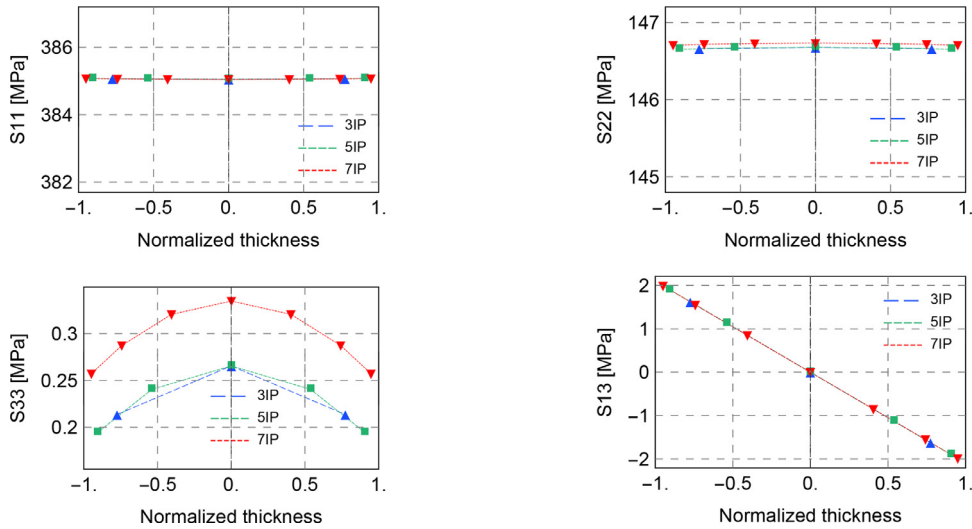
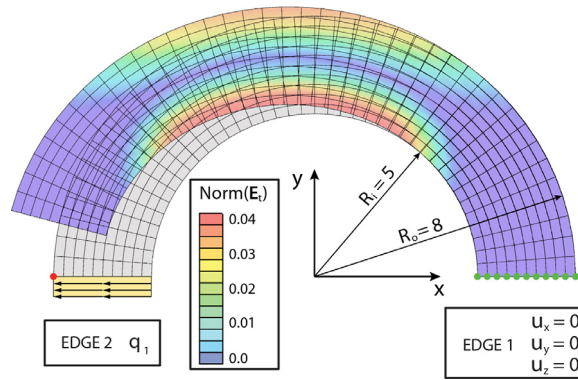**Fig. 11.** Through the thickness stress distribution for C3 and EAS element, at point P.

Fig. 12. Curved beam: geometry, mesh, boundary conditions (C3), loading, and deformed mesh with $||E_t||$ for C1 at $\lambda = 1$.

in this particular case) in regions where localized 3D effects may be expected. It also seems that such 3D effects are more pronounced when (volume preserving) transition takes place. However, this has a negligible influence on the global (stress resultant) level of the response. For example, C3 and C4 load-displacement curves in Fig. 10 are practically identical, and for C4, the only non-zero stress is S_{11}.

4.5. Curved beam

A curved beam with thickness $h = 1$ mm (see Fig. 12) is analyzed (after [35]) for four cases of boundary conditions (C1-C4), wherein the first three cases are the same as those in the previous example, while for C4 the point with coordinates $(R_o, 0, 0)$ is restrained as $u_x = u_y = u_z = 0$, and the rest of the edge 1 is restrained as $u_y = u_z = 0$. On edge 2, the line load $q_1 = q\lambda$ is applied, where $q = 60$ N/mm and λ is the load multiplier, which is increased from 0 to 1 and decreased back to 0. Set 2 of the material parameters and a regular mesh with 40 elements in the circumferential and 10 elements in the radial direction are used.

In Fig. 12, the amount of transformation in the middle surface is shown. Figure 13 shows the relation between the applied force and the displacement in the $-x$ direction of the point with the initial coordinates $(-R_o, 0, 0)$. The curves are compared with those from reference [35], where a mesh of 40×10 2D elements was used for a small-strain SMA, labelled as "Ref. SS", and for a large-strain SMA, labelled as "Ref. FS". As for the previous example, none of our curves matches the one from Evangelista et al. [35], indicating again that the 2D element in [35] is neither plane stress nor plane strain. The curves C2, C3 and C4 are similar, while the plane-strain curve C1 shows the stiffest response. For this example, there is no significant difference between C2 and C3 (and C4), in contrast with the previous example. In general, the EAS formulation is softer than the 2ANS and 3ANS.

It is worth noting that for the 2D tests presented in [36] (i.e., the first three examples), the results of our formulations match perfectly with those from Arghavani et al. [36]. On the other hand, for the 2D tests presented in [35] (i.e., this one
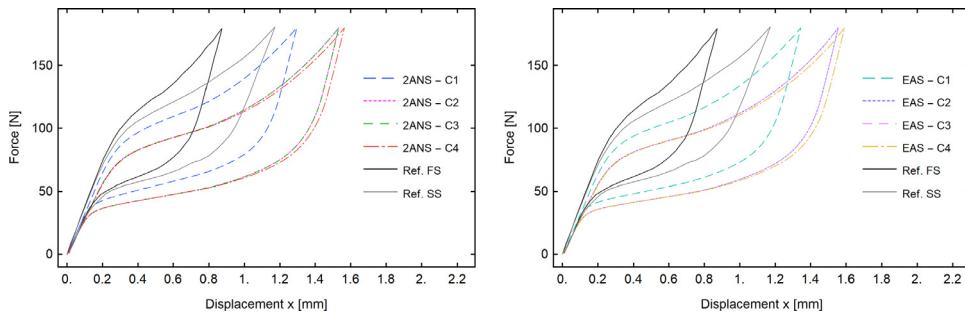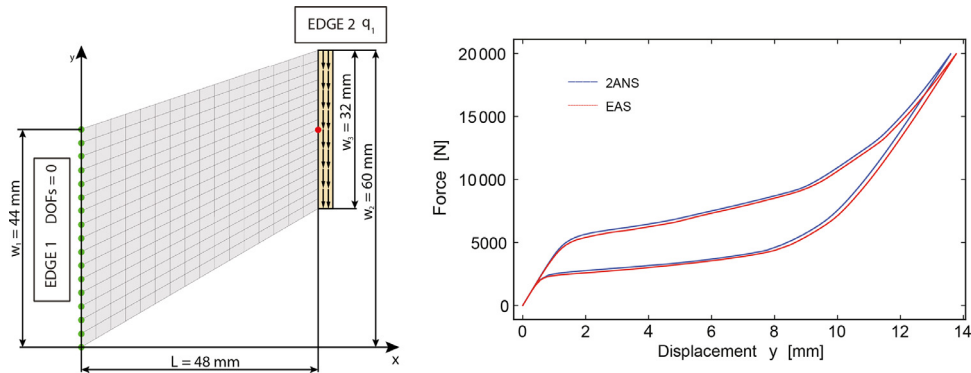
Fig. 13. Curved beam: superelastic response.

Fig. 14. Cook's membrane: geometry, mesh, boundary conditions and loading (left) and superelastic response(right).
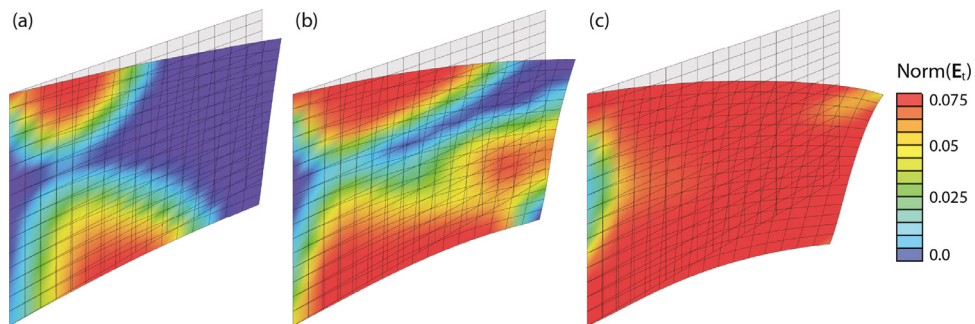

Fig. 15. Cook's membrane: initial and deformed 2ANS mesh at: (a) $\lambda = 0.35$, (b) $\lambda = 0.45$ and (c) $\lambda = 1$.

and the previous one), the results of our formulations do not match with those from Evangelista et al. [35]. We attribute the difference to the unknown 2D formulation in [35]. As shown in Section 4.8 for a 3D example, our results match perfectly with those from Evangelista et al. [35].

4.6. Cook's membrane

A Cook's membrane of length $L = 48$ mm and thickness $h = 1$ mm is considered (see Fig. 14 (left)). Edge 1 is fully clamped, i.e., all 7 degrees of freedom are set to 0. Load $q_1 = q\lambda$ is applied on edge 2, where $q = 625$ N/mm and λ is the load multiplier that goes from 0 to 1 and back to 0. A regular mesh of 16×16 elements and Set 1 of the material parameters are used.

Figure 14 (right) presents the relationship between the vertical reaction force on edge 1 and the displacement in the $-y$ direction for the middle point on edge 2. Figure 15 shows the initial and deformed meshes, along with the transformation strain norm $||\boldsymbol{E}_t||$ for the middle surface of 2ANS. The stress state through the thickness is not homogeneous due to the imposed boundary conditions on edge 1. Small differences between the three formulations are observable, and like previous examples, the EAS response is slightly softer.
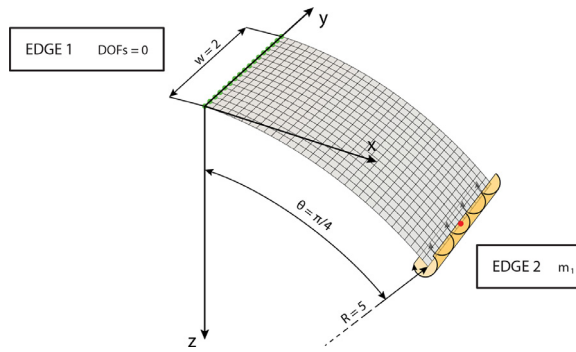
Fig. 16. Cylindrical panel: geometry, mesh, boundary conditions and loading.
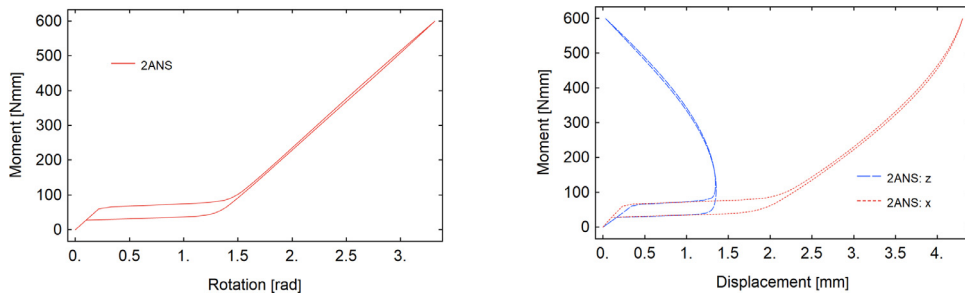

Fig. 17. Cylindrical panel: superelastic response presented by rotation (left) and by displacements (right).
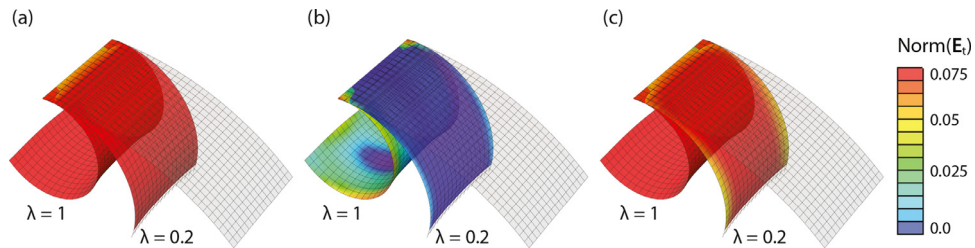

Fig. 18. Cylindrical panel: initial and deformed 2ANS meshes and transformation for: (a) "upper" surface, (b) middle surface, and (c) "lower" surface.

4.7. Bending of a cylindrical panel

A cylindrical panel with radius $R = 5$ mm, angle $\theta = \pi/4$, width $w = 2$ mm, and thickness $h = 0.5$ mm is subjected to a bending moment m_1 (see Fig. 16). Edge 1 is fully clamped, i.e., all 7 degrees of freedom are set to 0. Load $m_1 = m\lambda$ is applied on edge 2, where $m = 300$ Nmm/mm and λ is the load multiplier. A mesh with 32 elements in the bending direction and 16 elements in width direction is used. Loading and unloading is considered, where λ is changed from 0 to 1 and decreased back to 0. Set 1 of the material parameters is used. This is a pure bending test, while all the previous examples were pure membrane tests.

Figure 17 (left) shows the superelastic response of the cylindrical panel by presenting the relationship between rotation (around $-y$ axis) of the middle point on edge 2 and the reaction moment on edge 1. In order to show the ability of our algorithm to find solutions for fully transformed material, the value of the applied load is high. A solution is only possible to obtain by using the line-search method, when solving local equations at the Gauss points (see Section 2.2.2), with $\Delta\zeta_{limit} = 0.005$. Without applying the line search, the algorithm finds converged solutions only for the applied moments that are less than 200 Nmm. The superelastic response is shown in Fig. 17 (right), where displacements in $-x$ and $-z$ of the middle point on edge 2 are shown. The initial and deformed meshes for $\lambda = 0.2$ and $\lambda = 1$ are shown in Fig. 18, along with the amount of transformation. The "upper" and "lower" surfaces are located at $\pm 0.5\sqrt{3/5}\,h$ from the middle surface. The transformation at the "upper" and "lower" surfaces is not completely symmetric with respect to the middle surface due to slight curvature deformation in the shorter direction.
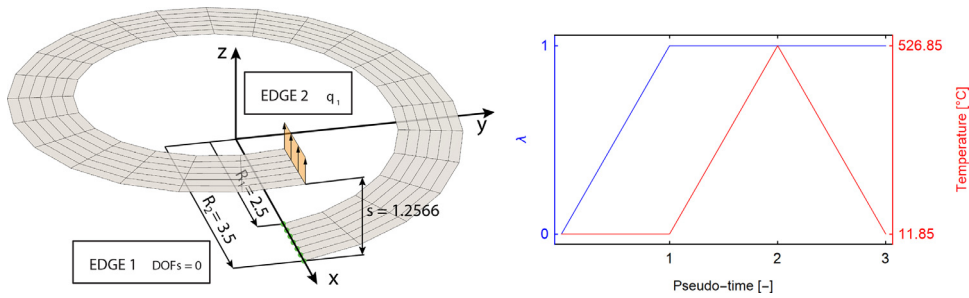
Fig. 19. Helical spring: geometry, mesh, boundary conditions and loading (left) and loading procedure (right).
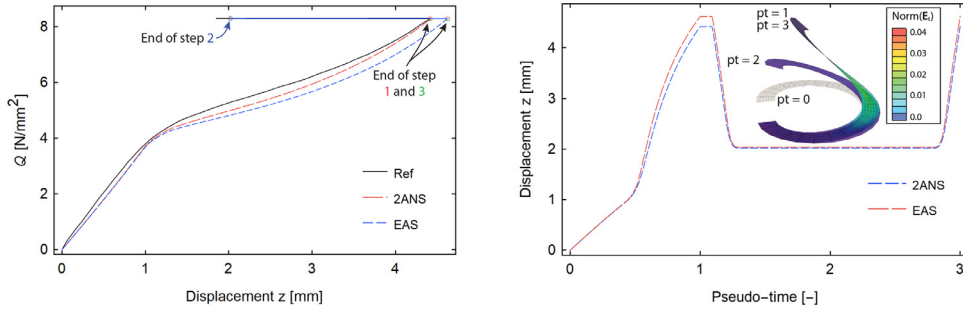

Fig. 20. Helical spring: superelastic response (left), displacement and deformed shape with indicated transformation during the loading (right).

4.8. Helical spring

A helical spring (see Fig. 19 (left)) of inner radius $R_1 = 2.5$ mm, outer radius $R_2 = 3.5$ mm, step $s = 1.2566$ mm, and thickness $h = 0.5$ mm is considered after [35]. Edge 1 is fully clamped, i.e., all degrees of freedom are 0, while edge 2 is subjected to load $q_1 = q\lambda$, where $q = 4.14$ N/mm and λ is the load multiplier. A regular mesh with 25 elements in the circumferential and 6 elements in the radial direction is used. Following [35], the mechanical and temperature loading are applied in three steps, where the duration of each step is 1 unit of dimensionless pseudo-time (see Fig. 19 (right)). The loading procedure is defined in the following way: (i) increase of λ from 0 to 1 at a constant ambient temperature of 11.85 °C, (ii) an increase of the temperature from 11.85 °C to 526.85 °C at $\lambda = 1$, and (iii) a decrease of the temperature back to 11.85 °C at $\lambda = 1$. Set 2 of the material parameters is used.

The relation between the average stress on edge 1, denoted as $\mathcal{Q}$, and the displacement in the $-z$ direction of the middle point on edge 2 is shown in Fig. 20 (left). The average stress is obtained by dividing the vertical reaction force by the cross-section area $(R_2 - R_1)h = 0.5$ mm². Our results are compared with those from Evangelista et al. [35], where a mesh of $25 \times 5 \times 5$ 8-node solid elements was used. Despite the small discrepancies, which might be because of the differences between the solid and shell formulations, meshes, and hyperelastic functions, our curves match well with the reference curves. For 2ANS, the maximum displacement at the end of the first loading step is almost identical with the reference curve, while at the end of the second step the difference in the displacements is 6.4%. The EAS formulation is softer than the 2ANS; therefore, the maximum displacement at the end of the first loading step is higher; however, the displacement change during the second loading step is similar to that of the reference curve. Fig. 20 (right) shows the displacement of the middle point on edge 2 during the loading procedure. At the end of the third step, when the temperature is back to the initial value, the displacement caused by the temperature change is also recovered. This is also seen in Fig. 20 (right), where the initial and deformed shapes at the end of each step for the 2ANS formulation are shown. Figure 21 presents distribution of stresses across the helical spring at the end of step (i) for EAS element. Stresses at the levels of the three through-the-thickness integration points are shown.

The order of S_{33} is rather high, roughly 1/10 of the order of other stresses. This is because the shell is not very thin, $h/R_2 = 1/7$, and due to slight 3D effects in more stressed part of the spring.

4.9. Half sphere

A half sphere of radius $r = 10$ mm, with a hole on top, angle $\theta = 2\pi/5$, and thickness $h = 0.4$ mm, is subjected to 2 point forces, see Fig. 22.

This is a standard benchmark test for shells, because of its response that couples the membrane and bending effects. Double symmetry is considered; therefore, only a quarter of the half sphere is analysed by taking into account the appropriate symmetry boundary conditions. In order to prevent rigid-body motion, the displacement of point P_0 with the coor-
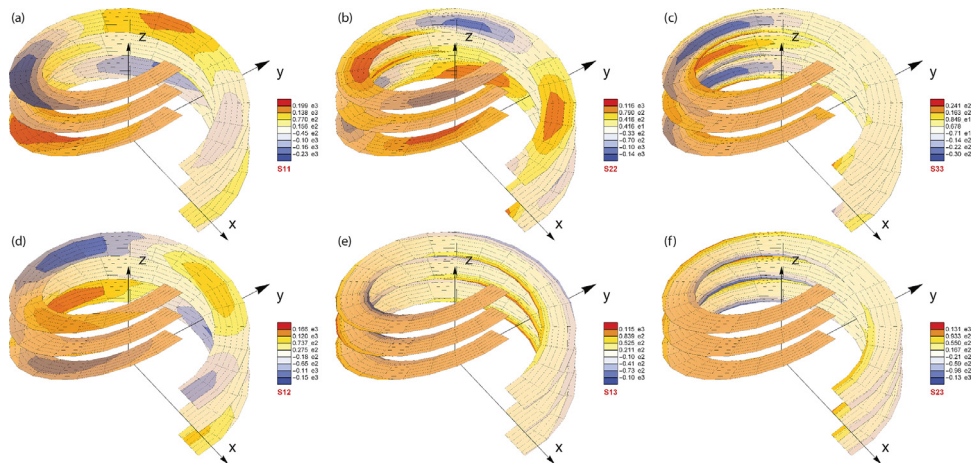
Fig. 21. Helical spring: Stress distribution at $\lambda = 1$ in "upper", middle and "lower" surface (for EAS element).
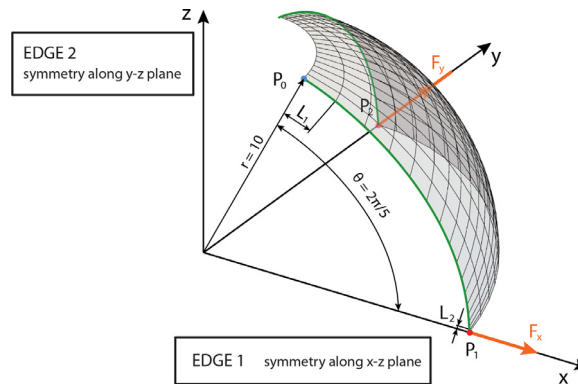

Fig. 22. Half sphere: geometry, distorted mesh (16×16), boundary conditions and loading.

dinates $(r \sin(\pi/10), 0, r \cos(\pi/10))$ is restrained in the z direction. At points $P_1 = (r, 0, 0)$ and $P_2 = (0, r, 0)$, forces $F_x = F\lambda$ and $F_y = F\lambda$ are applied, respectively, where $F = 100$ N and λ is the load multiplier.

Four cases with fine and coarse meshes are considered. The first and second cases (C1 and C2) have regular and distorted meshes with 4×4 elements, respectively. The third and fourth cases (C3 and C4) utilize regular and distorted meshes with 16×16 elements, respectively. The distorted meshes have the ratio $L_1/L_2 = 16$. Loading and unloading is considered by increasing λ from 0 to 1 and back to 0, and Set 1 of the material parameters is used.

Figure 23 shows the relationship between the force and the displacement of points P_1 and P_2 in the x and $-y$ directions, respectively. For finer meshes, the results for 2ANS and 3ANS and for both meshes are almost identical; therefore, only one curve is shown to represent all four analyses. Similarly, the difference between the regular and distorted finer meshes for the EAS are negligible. For the coarse meshes, the 3ANS results are much closer to the fine-mesh results than the 2ANS results, while the EAS results are the closest to the fine-mesh result. For the coarse regular (R) mesh, the difference between the 2ANS, 3ANS and EAS results is large. For the coarse distorted (D) mesh, the difference in the results between the 2AND and 3ANS is smaller. However, the EAS results are different. This is because of the way the distortion is applied (the mesh is finer in the vicinity of the forces). This example shows the advantage of 3ANS over 2ANS for shell problems where the interaction between the bending and membrane effects is present. The 3ANS and EAS give much better results for coarse and distorted meshes. In Table 2, u_x of point P_1 and u_y of point P_2 are collected for a particular load multiplier for all elements and meshes. Figure 24 shows the initial and deformed fine regular mesh at $\lambda = 1$. The amount of transformation is shown as well, with the "upper" and "lower" surfaces defined in the same way, with respect to the thickness, as in the Example 4.7 above. As expected, the transformation is not homogeneous through the thickness and a larger level of transformation is present in areas near the application of the forces.

4.10. Twisted beam

Similar to example in [84] a beam of length $L = 12$ mm and for 2π twisted along its axis, with width $w = 2$ mm and thickness $h = 0.2$ mm (see Fig. 25 (lower)) is analyzed. It has one edge clamped (i.e., all 7 degrees of freedom are 0 in this
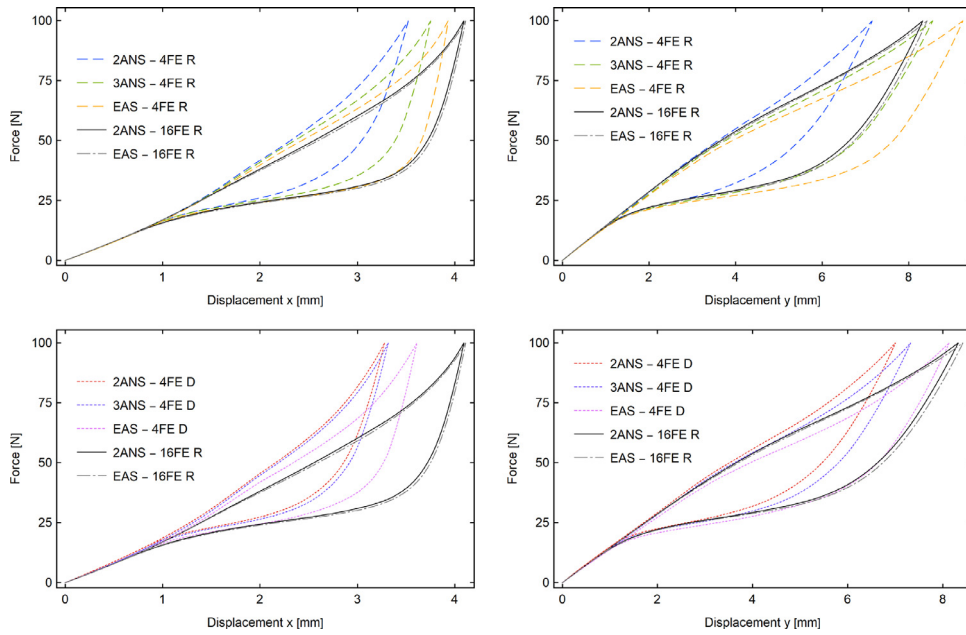
Fig. 23. Half sphere: force versus displacement curves.

Table 2
Displacements u_x (point P_1) and u_y (point P_2), in [mm], for a particular value of load multiplier.

| | | 2ANS | | | | | | 3ANS | | | | EAS | | | | | |
| | | 4 FE-R | | 4 FE-D | | 16 FE-R | | 4 FE-R | | 4 FE-D | | 4 FE-R | | 4 FE-D | | 16 FE-R | |
	λ	u_x	u_y	u_x	u_y	u_x	u_y	u_x	u_y	u_x	u_y	u_x	u_y	u_x	u_y	u_x	u_y
Loading	0.2	1.15	1.42	1.06	1.36	1.15	1.38	1.15	1.44	1.10	1.40	1.17	1.46	1.14	1.46	1.16	1.39
	0.4	1.93	2.80	1.81	2.73	2.09	2.83	1.96	2.90	1.84	2.80	2.01	3.00	1.93	2.98	2.12	2.86
	0.6	2.65	4.44	2.48	4.37	2.99	4.59	2.75	4.81	2.52	4.57	2.86	5.08	2.72	5.01	3.04	4.66
	0.8	3.17	5.98	2.97	5.91	3.70	6.69	3.38	6.92	3.01	6.22	3.56	7.47	3.28	6.93	3.72	6.74
	1	3.52	7.16	3.28	7.00	4.09	8.32	3.75	8.55	3.32	7.32	3.93	9.25	3.61	8.13	4.11	8.42
Unloading	0.8	3.38	6.62	3.15	6.51	3.98	7.78	3.64	7.96	3.19	6.83	3.84	8.71	3.50	7.64	4.00	7.88
	0.6	3.19	5.95	2.98	5.88	3.83	7.10	3.49	7.26	3.03	6.22	3.73	8.05	3.36	7.03	3.86	7.20
	0.4	2.80	4.80	2.65	4.85	3.52	5.92	3.18	6.02	2.72	5.20	3.50	6.91	3.07	5.96	3.56	6.03
	0.2	1.28	1.62	1.16	1.51	1.40	1.63	1.30	1.66	1.21	1.60	1.35	1.73	1.34	1.80	1.44	1.66
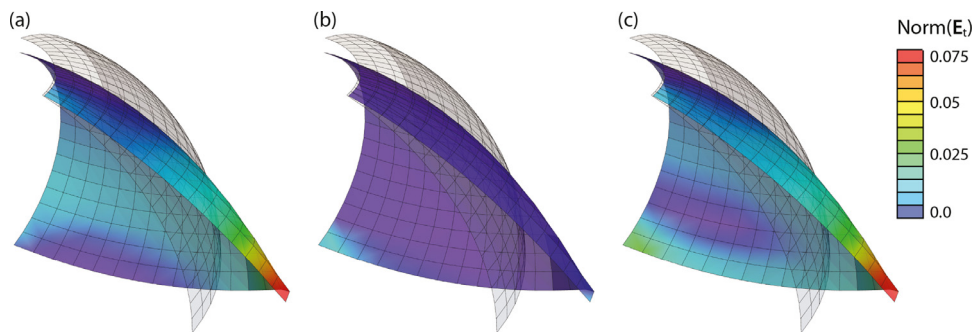
Fig. 24. Half sphere: initial and deformed 2ANS mesh with indicated level of transformation for: (a) "upper" surface, (b) middle surface points and (c) "lower" surface.

case). At the opposite edge, the axial displacement $u = u_{\max}\lambda$ is imposed, where $u_{\max} = 1.1$ mm and λ is load multiplier. Set 1 of material parameters is used for regular and distorted meshes, with 32 elements in longitudinal and 16 elements in the transverse direction. For the latter mesh, the ratio $r = L_1/L_2 = 1.1$ is applied (see Fig. 25 (upper)). For the regular mesh, the loading and unloading are considered through the displacement control, with increasing λ from 0 to 1 and decreasing it back to 0 in order to obtain a superelastic response. However, for the distorted mesh, the symmetry with respect to the beam axis is lost, which induces small geometric imperfections that trigger instability, and the arc length method [85] is
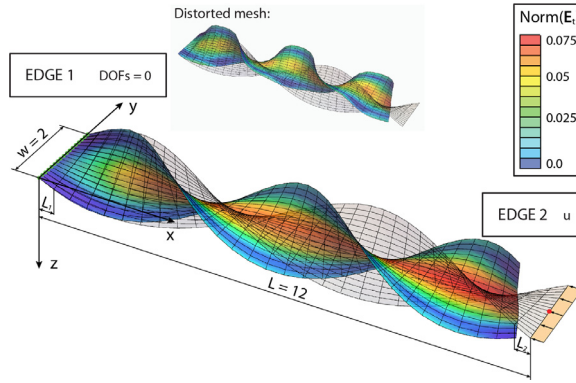
Fig. 25. Twisted beam: geometry, boundary conditions, loading (shown on initial (gray) regular mesh), and deformed configuration (in color) for 2ANS (lower), initial and deformed shape (distorted mesh) with transformation of mid-surface at maximal computed displacement for 2ANS (upper).
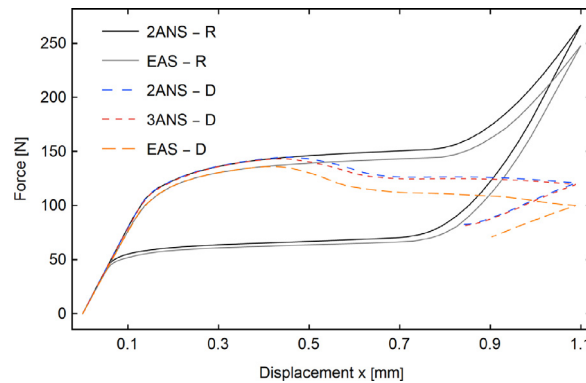

Fig. 26. Twisted beam: Superelastic response

used, which does not allow the control of loading and unloading by prescribing λ, because the latter becomes unknown that is computed in the solution process.

Figure 26 shows relationship between the reaction force on edge 1 and the displacement of the mid-point on edge 2, both in the $-x$ direction. It can be seen that for the regular mesh, the loading and unloading generate superelastic responses without any instability. A deformed regular mesh is shown in Fig. 25 (lower) for $\lambda = 0.65$, with colours indicating the amount of transformation in the mid-surface (we can see the symmetry of the transformation with respect to the mid-axis). This is in contrast with the results for the distorted mesh, when buckling occurs, for the 2ANS and 3ANS elements at approximately 0.5 mm and for the EAS element at approximately 0.4 mm. The arc-length starts with unloading at some point, but the algorithm is not able to find much of the subsequent solution path. Figure 25 (upper) shows the deformed distorted mesh at the maximum displacement. This example illustrates how small imperfections (induced here simply with a mesh distortion) generate very different results for a buckling-sensitive SMA.

4.11. Tube in tension

A cylinder of length $L = 30$ mm, mid-diameter $d = 4.326$ mm and thickness $h = 0.348$ mm is subjected to axial tension, see Fig. 27 (left). On both edges, all degrees of freedom are set to 0, except for axial displacement at edge 2, which is $u = u_{max}\lambda$, where $u_{max} = 1.1$ mm and λ is load multiplier. Loading and unloading is considered by increasing λ from 0 to 1 and back to 0. Regular mesh with 40×40 elements is used. The main purpose of this example is identification of material parameters by comparing our results with experimental data from Helm and Haupt [83], and use these parameters to compute the next example. The calibration yielded Set 3 data given in (90) for the ambient temperature $T = 27.5\,°$C, which was roughly the average temperature during the experiment. Figure 27 (right) shows our results (with Set 3 data), experimental results [83] and numerical solution [41] with 3D solid finite element. Axial stress is $\sigma = F/A$, where F is axial reaction force and A is initial cross section area. Axial strain is $\varepsilon = \Delta l/l$, where Δl is displacement difference between the nodes initially at $z = 15$ mm ± 0.75 mm and l is the initial distance between these nodes (i.e. 1.5 mm). Some discrepancies are present between our curves and the experiment curve ("Ref. Exp"), while differences between our curves and the curve from Reese and Christ [41] ("Ref. Sim") are minor. At the beginning of the martensite transformation and at the end of the reverse transformation our curves are non-smooth because of nucleation and completion condition.
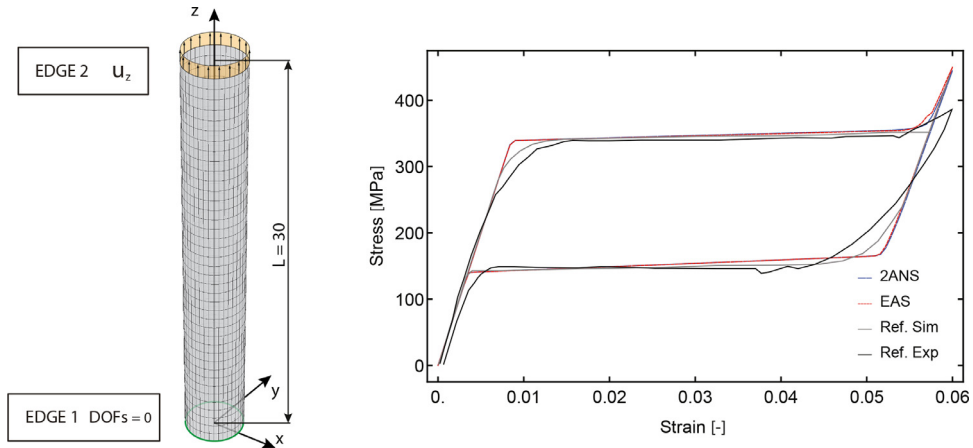
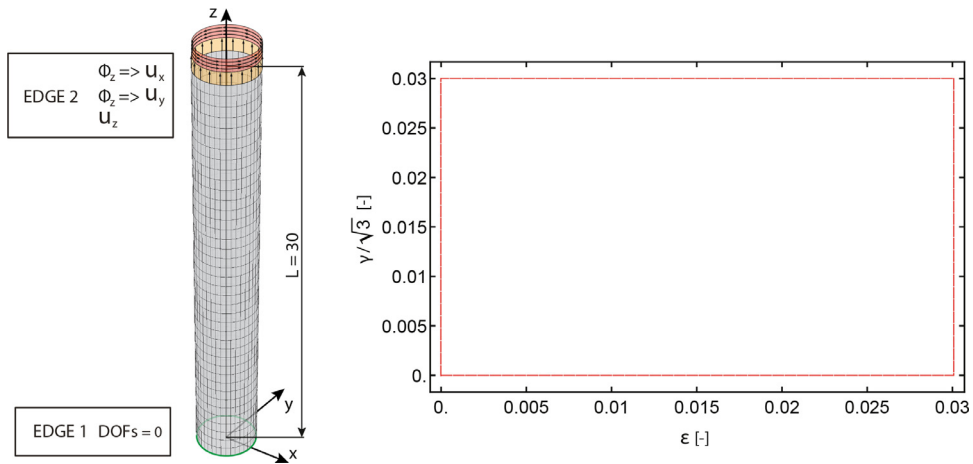**Fig. 27.** Tube in tension: geometry, boundary conditions, loading (left), and superelastic response (right).

Fig. 28. Tube in tension and torsion: geometry, boundary conditions, loading (left), and load path (right).

4.12. Tube in tension and torsion

The cylinder from the previous example is subjected to tension and torsion, after [83] and [41], see Fig. 28. Edge 1 is clamped (i.e. all degrees of freedom are 0), while edge 2 is subjected to axial stretching $u_z = u_{max} \lambda_1$ followed by torsion $\phi_z = \phi_{max} \lambda_2$, where λ_1 and λ_2 are load multipliers. Torsional rotation is applied by imposing u_x and u_y due to ϕ_z. The thickness change and the director rotations (i.e. 4th to 7th degrees of freedom) are set to 0 on edge 2. The $u_{max} = 0.903$ and $\phi_{max} = 0.722$ are such that 3% normal and shear deformations are reached, with normal deformation defined as $\varepsilon = \Delta L/L$ (where ΔL is axial displacement on edge 2) and shear deformation defined as $\gamma/\sqrt{3}$, where $\gamma = (\phi_z d)/(2L)$. Loading consists of 4 steps: (i) λ_1 is increasing from 0 to 1 at $\lambda_2 = 0$, (ii) λ_2 is increasing from 0 to 1 at $\lambda_1 = 1$, (iii) λ_1 is decreasing from 1 to 0 at $\lambda_2 = 1$, and (iv) λ_2 is decreasing from 1 to 0 at $\lambda_1 = 0$. Regular mesh with 40×40 elements and Set 3 material parameters are used.

Figure 29 (left) compares our results with experimental results [83] ("Ref. Exp") and simulation from Reese and Christ [41] ("Ref. Sim"), in which 3D solid elements were used. In Fig. 29 (left), $\sigma = F/A$, where F is axial reaction force and A is initial cross section area, and $\tau = (Md/2)/(\pi/32(D_{out}^4 - D_{in}^4))$, where M is torsional moment and D_{in} and D_{out} are the inner and the outer diameter of the tube, respectively. The match of our curve to the experiment and the reference simulation is acceptable, although not perfect. The main reason for the differences between the simulations (2ANS and "Ref. Sim") are different constitutive equations used. However, both simulations lack the compression-tension asymmetry, which may be the reason for the deviations from the experiment. Another significant difference between the experiment and simulations is temperature change of the material. In [83], temperature changes are measured during the experiments, indicating non-isothermal conditions, whereas in simulations isothermal loading is considered. Figure 29 (right) shows distribution of the transformation, which is similar as in [41]. Figure 30 compares normal and shear stress-strain curves with experiment [83]. Normal stress-strain curve matches well the experiment, especially in the first and the second loading step, while the
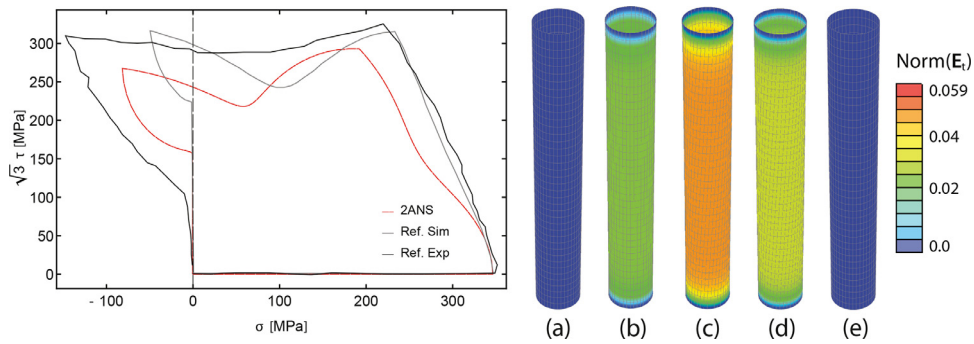
Fig. 29. Tube in tension and torsion: superelastic response (left) and transformation of the mid-surface (right): (a) initial state, (b) end of step (i), (c) end of step (ii), (d) end of step (iii) and (e) end of step (iv).
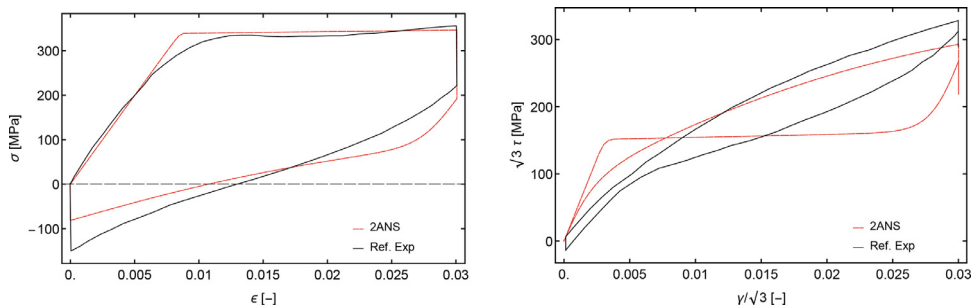

Fig. 30. Tube in tension and torsion: superelastic response presented with normal (left) and shear (right) stress-strain relation.

matching for the shear stress-strain curve is worse. We assume that the main reason is temperature change of the sample as a consequence of transformation during the experiment. Namely, the temperature increase at loading steepens the slope of the curve during transformation.

5. Conclusions

In this work we have derived, for the first time, a shell finite element formulation for the simulation of deformations of thin-walled shape-memory alloys under mechanical and thermal loadings. Such formulations are much more suited to thin-walled and curved SMA structures than solid finite element formulations, which can have difficulties correctly representing the bending and buckling of the shell-like structures. As for the SMA material model, we revised the finite strain model presented in [35] and [36]. Novel approaches related to its efficient finite element implementation are described. As for the shell finite element formulations, we have applied a seven-parameter shell model and three corresponding finite elements that extensively use an assumed natural strain and enhanced assumed strain enhancements. Although only one formulation can fulfill the condition of the zero-through-the-thickness normal stress, and the other two can do that only approximately, the corresponding load-displacement curves differ only slightly. Also, although the formulation with the enhanced assumed strain enhancements can approximate better the incompressibility of the transformation strains, its results do not differ much from the formulations with the assumed natural strain formulations.

Numerical examples show that for an excellent match for the results obtained with the solid SMA formulation, the number of elements needed for the shell SMA model is less than 25% of the number of elements needed for the solid SMA model. We believe that for thin-walled SMAs the same (or even superior) accuracy of the results can be obtained with shell formulations in comparison with solid formulations, for a considerably reduced number of elements in the mesh, and for a significant reduction in the computational time. Moreover, two of the applied shell finite element formulations, i.e. 3ANS and EAS, are designed to be low-sensitive with respect to mesh distortion, which can further reduce the necessary number of elements in the mesh.

Although the numerical simulations offer the rapid generation of results, great attention is required for the determination of the input-material parameters to obtain reliable results. The process of determination for the SMA material parameters from experiments is trivial for small strain formulations, whereas for finite strain formulations more caution is needed, since the finite strain material models include a differentiation between the (reference, intermediate and current) configurations. Therefore, our future work will involve finite strain SMA material parameter determinations as part of developing opportunities for an enhancement of the current SMA shell formulation, e.g., a smooth transition of the thermomechanical response at the beginning and the end of the phase transformation and a consideration of the compression-tension asymmetry.

Declaration of Competing Interest

The authors declare that they have no known competing financial interests or personal relationships that could have appeared to influence the work reported in this paper.

CRediT authorship contribution statement

Luka Porenta: Software, Investigation, Validation, Writing - original draft. **Marko Lavrenčič:** Software, Investigation. **Jaka Dujc:** Software, Validation. **Miha Brojan:** Conceptualization, Writing - review & editing. **Jaka Tušek:** Funding acquisition, Writing - review & editing. **Boštjan Brank:** Conceptualization, Methodology, Supervision, Writing - review & editing.

Acknowledgments

Appendix A

$$\dot{\boldsymbol{E}} = \frac{1}{2}\dot{\boldsymbol{C}} = \frac{1}{2}\left(\dot{\boldsymbol{F}}^{\mathrm{T}}\boldsymbol{F} + \boldsymbol{F}^{\mathrm{T}}\dot{\boldsymbol{F}}\right) = \frac{1}{2}\left(\boldsymbol{F}^{\mathrm{T}}\underbrace{\boldsymbol{F}^{-\mathrm{T}}\dot{\boldsymbol{F}}^{\mathrm{T}}}_{\boldsymbol{L}^{\mathrm{T}}}\boldsymbol{F} + \boldsymbol{F}^{\mathrm{T}}\underbrace{\dot{\boldsymbol{F}}\boldsymbol{F}^{-1}}_{\boldsymbol{L}}\boldsymbol{F}\right) = \frac{1}{2}\boldsymbol{F}^{\mathrm{T}}\left(\boldsymbol{L} + \boldsymbol{L}^{\mathrm{T}}\right)\boldsymbol{F} = \boldsymbol{F}^{\mathrm{T}}\boldsymbol{d}\,\boldsymbol{F} \tag{A.1}$$

$$\det(\boldsymbol{F}_t) = J_t = 1 \Rightarrow \dot{J}_t = 0$$
$$\dot{J}_t = \frac{\partial J_t}{t} = \frac{\partial J_t}{\boldsymbol{F}_t} : \frac{\partial \boldsymbol{F}_t}{t} = \frac{\partial \det(\boldsymbol{F}_t)}{\boldsymbol{F}_t} : \dot{\boldsymbol{F}}_t = J_t \boldsymbol{F}_t^{-\mathrm{T}} : \dot{\boldsymbol{F}}_t = J_t \operatorname{tr}\left(\boldsymbol{F}_t^{-\mathrm{T}}\dot{\boldsymbol{F}}_t^{\mathrm{T}}\right) = J_t \operatorname{tr}\left(\dot{\boldsymbol{F}}_t\boldsymbol{F}_t^{-1}\right) =$$
$$= J_t \operatorname{tr}(\boldsymbol{L}_t) = J_t \operatorname{tr}(\boldsymbol{d}_t + \boldsymbol{w}_t) = J_t(\operatorname{tr}(\boldsymbol{d}_t) + \operatorname{tr}(\boldsymbol{w}_t)) = J_t \operatorname{tr}(\boldsymbol{d}_t) \Rightarrow \operatorname{tr}(\boldsymbol{d}_t) = 0 \tag{A.2}$$

$$\dot{\boldsymbol{C}}_e = \dot{\boldsymbol{F}}_t^{-T}\boldsymbol{C}\boldsymbol{F}_t^{-1} + \boldsymbol{F}_t^{-T}\dot{\boldsymbol{C}}\boldsymbol{F}_t^{-1} + \boldsymbol{F}_t^{-T}\boldsymbol{C}\dot{\boldsymbol{F}}_t^{-1} = \underbrace{\dot{\boldsymbol{F}}_t^{-T}\boldsymbol{F}_t^{\mathrm{T}}}_{\boldsymbol{L}_t^{-\mathrm{T}}}\boldsymbol{C}_e\underbrace{\boldsymbol{F}_t\boldsymbol{F}_t^{-1}}_{1} + \boldsymbol{F}_t^{-T}\dot{\boldsymbol{C}}\boldsymbol{F}_t^{-1} + \underbrace{\boldsymbol{F}_t^{-T}\boldsymbol{F}_t^{\mathrm{T}}}_{1}\boldsymbol{C}_e\underbrace{\boldsymbol{F}_t\dot{\boldsymbol{F}}_t^{-1}}_{\boldsymbol{L}_t^{-1}} =$$
$$= -\boldsymbol{L}_t^{\mathrm{T}}\boldsymbol{C}_e + \boldsymbol{F}_t^{-T}\dot{\boldsymbol{C}}\boldsymbol{F}_t^{-1} - \boldsymbol{C}_e\boldsymbol{L}_t \tag{A.3}$$

$$\boldsymbol{S} : \frac{1}{2}\dot{\boldsymbol{C}} - \frac{\partial \psi_e}{\boldsymbol{C}_e} : \dot{\boldsymbol{C}}_e = \boldsymbol{S} : \frac{1}{2}\dot{\boldsymbol{C}} - \frac{\partial \psi_e}{\boldsymbol{C}_e} : \left(-\boldsymbol{L}_t^{\mathrm{T}}\boldsymbol{C}_e + \boldsymbol{F}_t^{-T}\dot{\boldsymbol{C}}\boldsymbol{F}_t^{-1} - \boldsymbol{C}_e\boldsymbol{L}_t\right) =$$
$$= \boldsymbol{S} : \frac{1}{2}\dot{\boldsymbol{C}} - \frac{\partial \psi_e}{\boldsymbol{C}_e} : \left(\boldsymbol{F}_t^{-T}\dot{\boldsymbol{C}}\boldsymbol{F}_t^{-1}\right) + 2\frac{\partial \psi_e}{\boldsymbol{C}_e} : (\boldsymbol{C}_e\boldsymbol{L}_t) =$$
$$= \boldsymbol{S} : \frac{1}{2}\dot{\boldsymbol{C}} - \boldsymbol{F}_t^{-1}\frac{\partial \psi_e}{\boldsymbol{C}_e}\boldsymbol{F}_t^{-T} : \dot{\boldsymbol{C}} + 2\boldsymbol{C}_e\frac{\partial \psi_e}{\boldsymbol{C}_e} : \boldsymbol{L}_t =$$
$$= \underbrace{\left(\boldsymbol{S} - 2\boldsymbol{F}_t^{-1}\frac{\partial \psi_e}{\boldsymbol{C}_e}\boldsymbol{F}_t^{-T}\right) : \frac{1}{2}\dot{\boldsymbol{C}}}_{1} + \underbrace{2\boldsymbol{C}_e\frac{\partial \psi_e}{\boldsymbol{C}_e} : \boldsymbol{L}_t}_{2} \tag{A.4}$$

$$\boldsymbol{X} = \tau_M \frac{\partial ||\boldsymbol{E}_t||}{\boldsymbol{E}_t} + \frac{1}{2}h\frac{\partial ||\boldsymbol{E}_t||^2}{\boldsymbol{E}_t} + \frac{\partial \mathscr{I}(||\boldsymbol{E}_t||)}{\boldsymbol{E}_t} = \tau_M \frac{\partial \sqrt{\operatorname{tr}(\boldsymbol{E}_t^2)}}{\boldsymbol{E}_t} + \frac{1}{2}h\frac{\partial \operatorname{tr}(\boldsymbol{E}_t^2)}{\boldsymbol{E}_t} + \frac{\partial \mathscr{I}(||\boldsymbol{E}_t||)}{\boldsymbol{E}_t} =$$
$$= \tau_M \frac{2\boldsymbol{E}_t^{\mathrm{T}}}{2\sqrt{\operatorname{tr}(\boldsymbol{E}_t^2)}} + \frac{1}{2}h\,2\boldsymbol{E}_t^{\mathrm{T}} + \frac{\partial \mathscr{I}(||\boldsymbol{E}_t||)}{\boldsymbol{E}_t} = \tau_M \frac{\boldsymbol{E}_t}{||\boldsymbol{E}_t||} + h\boldsymbol{E}_t + \gamma \underbrace{\frac{\boldsymbol{E}_t}{||\boldsymbol{E}_t||}}_{\boldsymbol{N}} \tag{A.5}$$

$$\boldsymbol{F}_t^{\mathrm{T}}(\boldsymbol{P} - \boldsymbol{K})\boldsymbol{F}_t = \boldsymbol{F}_t^{\mathrm{T}}\boldsymbol{P}\boldsymbol{F}_t - \boldsymbol{F}_t^{\mathrm{T}}\boldsymbol{K}\boldsymbol{F}_t = \boldsymbol{F}_t^{\mathrm{T}}2\boldsymbol{C}_e\underbrace{\frac{1}{\boldsymbol{F}_t\boldsymbol{F}_t^{-1}}}_{}\frac{\partial \psi_e}{\boldsymbol{C}_e}\underbrace{\frac{1}{\boldsymbol{F}_t^{-T}\boldsymbol{F}_t^{\mathrm{T}}}}_{}\boldsymbol{F}_t - \boldsymbol{F}_t^{\mathrm{T}}\boldsymbol{F}_t\,\boldsymbol{X}\,\underbrace{\boldsymbol{F}_t^{\mathrm{T}}\boldsymbol{F}_t}_{\boldsymbol{C}_t} =$$
$$= \underbrace{\boldsymbol{F}_t^{\mathrm{T}}\boldsymbol{C}_e\boldsymbol{F}_t}_{\boldsymbol{C}}\underbrace{2\boldsymbol{F}_t^{-1}\frac{\partial \psi_e}{\boldsymbol{C}_e}\boldsymbol{F}_t^{-T}}_{\boldsymbol{S}}\underbrace{\boldsymbol{F}_t^{\mathrm{T}}\boldsymbol{F}_t}_{\boldsymbol{C}_t} - \boldsymbol{C}_t\,\boldsymbol{X}\,\boldsymbol{C}_t = (\boldsymbol{C}\boldsymbol{S} - \boldsymbol{C}_t\,\boldsymbol{X})\,\boldsymbol{C}_t = \boldsymbol{Y}\,\boldsymbol{C}_t \tag{A.6}$$

$$\boldsymbol{F}_t^{\mathrm{T}}(\boldsymbol{P} - \boldsymbol{K})^{\mathrm{D}}\boldsymbol{F}_t = \boldsymbol{F}_t^{\mathrm{T}}\left(\boldsymbol{P} - \boldsymbol{K} - \frac{1}{3}\operatorname{tr}(\boldsymbol{P} - \boldsymbol{K})\,\boldsymbol{1}\right)\boldsymbol{F}_t = \underbrace{\boldsymbol{F}_t^{\mathrm{T}}(\boldsymbol{P} - \boldsymbol{K})\boldsymbol{F}_t}_{\boldsymbol{Y}\boldsymbol{C}_t} - \frac{1}{3}\operatorname{tr}(\boldsymbol{P} - \boldsymbol{K})\underbrace{\boldsymbol{F}_t^{\mathrm{T}}\boldsymbol{F}_t}_{\boldsymbol{C}_t} =$$

$$= \boldsymbol{Y}\boldsymbol{C}_t - \frac{1}{3}\text{tr}\left(2\underbrace{\boldsymbol{C}_e}_{\boldsymbol{F}_t^{-\text{T}}\boldsymbol{C}\boldsymbol{F}_t^{-1}}\frac{\partial\psi_e}{\boldsymbol{C}_e} - \boldsymbol{F}_t\boldsymbol{X}\boldsymbol{F}_t^{\text{T}}\right)\boldsymbol{C}_t = \boldsymbol{Y}\boldsymbol{C}_t - \frac{1}{3}\text{tr}\left(\boldsymbol{F}_t^{-\text{T}}\boldsymbol{C}\underbrace{\boldsymbol{F}_t^{-1}\boldsymbol{F}_t}_{1}\underbrace{2\boldsymbol{F}_t^{-1}\frac{\partial\psi_e}{\boldsymbol{C}_e}\boldsymbol{F}_t^{-\text{T}}}_{\boldsymbol{S}}\boldsymbol{F}_t^{\text{T}} - \right.$$

$$\left. -\boldsymbol{F}_t^{-\text{T}}\underbrace{\boldsymbol{F}_t^{\text{T}}\boldsymbol{F}_t}_{\boldsymbol{C}_t}\boldsymbol{X}\underbrace{\boldsymbol{F}_t^{\text{T}}\boldsymbol{F}_t}_{\boldsymbol{C}_t}\boldsymbol{F}_t^{-1}\right)\boldsymbol{C}_t = \boldsymbol{Y}\boldsymbol{C}_t - \frac{1}{3}\text{tr}\left(\underbrace{\boldsymbol{F}_t^{\text{T}}\boldsymbol{F}_t^{-\text{T}}}_{1}\boldsymbol{C}\boldsymbol{S} - \boldsymbol{C}\boldsymbol{S} - \overbrace{\boldsymbol{F}_t^{-1}\boldsymbol{F}_t^{-\text{T}}}^{1}\underbrace{\boldsymbol{C}_t}_{\boldsymbol{C}_t^{-1}}\boldsymbol{X}\boldsymbol{C}_t\right)\boldsymbol{C}_t =$$

$$= \boldsymbol{Y}\boldsymbol{C}_t - \frac{1}{3}\text{tr}\left(\underbrace{\boldsymbol{C}\boldsymbol{S} - \boldsymbol{C}_t\boldsymbol{X}}_{\boldsymbol{Y}}\right)\boldsymbol{C}_t = \boldsymbol{Y}^{\text{D}}\boldsymbol{C}_t \tag{A.7}$$

$$\|\boldsymbol{Z}^{\text{D}}\| = \|(\boldsymbol{P}-\boldsymbol{K})^{\text{D}}\| = \|\boldsymbol{F}_t^{-\text{T}}\boldsymbol{Y}^{\text{D}}\boldsymbol{F}_t^{\text{T}}\| = \sqrt{\text{tr}\left(\boldsymbol{F}_t^{-\text{T}}\boldsymbol{Y}^{\text{D}}\underbrace{\boldsymbol{F}_t^{\text{T}}\boldsymbol{F}_t}_{\boldsymbol{C}_t}\boldsymbol{Y}^{\text{DT}}\boldsymbol{F}_t^{-1}\right)} =$$

$$= \sqrt{\text{tr}\left(\underbrace{\boldsymbol{F}_t^{-1}\boldsymbol{F}_t^{-\text{T}}}_{\boldsymbol{C}_t^{-1}}\boldsymbol{Y}^{\text{D}}\underbrace{\boldsymbol{C}_t\boldsymbol{Y}^{\text{DT}}}_{\boldsymbol{Y}^{\text{D}}\boldsymbol{C}_t}\right)} = \sqrt{\text{tr}\left(\underbrace{\boldsymbol{C}_t\boldsymbol{C}_t^{-1}}_{1}\boldsymbol{Y}^{\text{D}}\boldsymbol{Y}^{\text{D}}\right)} = \sqrt{\boldsymbol{Y}^{\text{D}}:\boldsymbol{Y}^{\text{DT}}} \neq \|\boldsymbol{Y}^{\text{D}}\| \tag{A.8}$$

References

[1] Jani JM, Leary M, Subic A, Gibson MA. A review of shape memory alloy research, applications and opportunities. Mater Des (1980-2015) 2014;56:1078–113.

[2] Brojan M, Bombač D, Kosel F, Videnič T. Shape memory alloys in medicine. RMZ-MaterGeoenvironment 2008;2(55):173–89.

[3] Petrini L, Migliavacca F. Biomedical applications of shape memory alloys. J Metall 2011;2011.

[4] Song C. History and current situation of shape memory alloys devices for minimally invasive surgery. Open Med Devices J 2010;2(1).

[5] Coral W, Rossi C, Colorado J, Lemus D, Barrientos A. SMA-based muscle-like actuation in biologically inspired robots: a state of the art review. In: Smart actuation and sensing systems-recent advances and future challenges; 2012. p. 53–82.

[6] Schetky LM. Shape memory alloy applications in space systems. Mater Des 1991;12(1):29–32.

[7] Hartl D, Mooney J, Lagoudas D, Calkins F, Mabe J. Use of a Ni60Ti shape memory alloy for active jet engine chevron application: II. Experimentally validated numerical analysis. Smart Mater Struct 2009;19(1):015021.

[8] Sofla A, Meguid S, Tan K, Yeo W. Shape morphing of aircraft wing: Status and challenges. Mater Des 2010;31(3):1284–92.

[9] Ozbulut O, Hurlebaus S, Desroches R. Seismic response control using shape memory alloys: a review. J Intell Mater SystStruct 2011;22(14):1531–49.

[10] Kaneko K, Enomoto K. Development of reciprocating heat engine using shape memory alloy-ratchet type drive system with self-drive rotational valve. J Envir Eng 2011;6(1):131–9.

[11] Tušek J, Engelbrecht K, Eriksen D, DallOlio S, Tušek J, Pryds N. A regenerative elastocaloric heat pump. Nat Energy 2016;1(10):1–6.

[12] Kabirifar P, Žerovnik A, Ahčin Ž, Porenta L, Brojan M, Tušek J. Elastocaloric cooling: state-of-the-art and future challenges in designing regenerative elastocaloric devices.. Strojniski Vestnik/J MechEng 2019;65.

[13] VHK and ARMINES. Technology roadmap in preparatory/review study on commission regulation (EC) no. 643/2009 with regard to ecodesign requirements for household refrigeration appliances and commission delegated regulation (eu) no. 1060/2010 with regard to energy labelling. www.ecodesign-fridges.eu; 2016.

[14] Ball JM, James RD. Fine phase mixtures as minimizers of energy. In: Analysis and continuum mechanics. Springer; 1989. p. 647–86.

[15] Zhong Y, Zhu T. Phase-field modeling of martensitic microstructure in NiTi shape memory alloys. Acta Mater 2014;75:337–47.

[16] Sadjadpour A, Bhattacharya K. A micromechanics inspired constitutive model for shape-memory alloys: the one-dimensional case. Smart Mater Struct 2007;16(1):S51.

[17] Lexcellent C, Vivet A, Bouvet C, Calloch S, Blanc P. Experimental and numerical determinations of the initial surface of phase transformation under biaxial loading in some polycrystalline shape-memory alloys. J Mech Phys Solids 2002;50(12):2717–35.

[18] Liang C, Rogers CA. One-dimensional thermomechanical constitutive relations for shape memory materials. J Intell Mater SystStruct 1997;8(4):285–302.

[19] Lagoudas DC, Bo Z, Qidwai MA. A unified thermodynamic constitutive model for SMA and finite element analysis of active metal matrix composites. Mech Compos Mater Struct 1996;3(2):153–79.

[20] Qidwai M, Lagoudas D. On thermomechanics and transformation surfaces of polycrystalline NiTi shape memory alloy material. Int J Plast 2000;16(10–11):1309–43.

[21] Bouvet C, Calloch S, Lexcellent C. A phenomenological model for pseudoelasticity of shape memory alloys under multiaxial proportional and nonpro-portional loadings. Eur J Mech-A/Solids 2004;23(1):37–61.

[22] Dhote R, Fabrizio M, Melnik R, Zu J. Hysteresis phenomena in shape memory alloys by non-isothermal Ginzburg–Landau models. Commun Nonlinear Sci NumerSimul 2013;18(9):2549–61.

[23] Zaki W, Moumni Z. A three-dimensional model of the thermomechanical behavior of shape memory alloys. J Mech Phys Solids 2007;55(11):2455–90.

[24] Popov P, Lagoudas DC. A 3-D constitutive model for shape memory alloys incorporating pseudoelasticity and detwinning of self-accommodated martensite. Int J Plast 2007;23(10–11):1679–720.

[25] Panico M, Brinson LC. A three-dimensional phenomenological model for martensite reorientation in shape memory alloys. J Mech Phys Solids 2007;55(11):2491–511.

[26] Chemisky Y, Duval A, Patoor E, Zineb TB. Constitutive model for shape memory alloys including phase transformation, martensitic reorientation and twins accommodation. Mech Mater 2011;43(7):361–76.

[27] Lagoudas DC, Entchev PB. Modeling of transformation-induced plasticity and its effect on the behavior of porous shape memory alloys. Part I: consti-tutive model for fully dense SMAs. Mech Mater 2004;36(9):865–92.

[28] Zaki W, Moumni Z. A 3D model of the cyclic thermomechanical behavior of shape memory alloys. J Mech Phys Solids 2007;55(11):2427–54.

[29] Morin C, Moumni Z, Zaki W. Thermomechanical coupling in shape memory alloys under cyclic loadings: experimental analysis and constitutive mod-eling. Int J Plast 2011;27(12):1959–80.

[30] Auricchio F, Sacco E. Thermo-mechanical modelling of a superelastic shape-memory wire under cyclic stretching–bending loadings. Int J Solids Struct 2001;38(34–35):6123–45.

[31] Zhu S, Zhang Y. A thermomechanical constitutive model for superelastic SMA wire with strain-rate dependence. Smart Mater Struct 2007;16(5):1696.

[32] Moussa MO, Moumni Z, Doare O, Touze C, Zaki W. Non-linear dynamic thermomechanical behaviour of shape memory alloys. J Intell Mater SystStruct 2012;23(14):1593–611.

[33] Ziolkowski A. Three-dimensional phenomenological thermodynamic model of pseudoelasticity of shape memory alloys at finite strains. Continuum Mech Thermodyn 2007;19(6):379–98.

[34] Helm D. Thermomechanics of martensitic phase transitions in shape memory alloys, I: constitutive theories for small and large deformations. J Mech Mater Struct 2007;2(1):87–112.

[35] Evangelista V, Marfia S, Sacco E. A 3D SMA constitutive model in the framework of finite strain. Int J Numer MethodsEng 2010;81(6):761–85.

[36] Arghavani J, Auricchio F, Naghdabadi R, Reali A. On the robustness and efficiency of integration algorithms for a 3D finite strain phenomenological SMA constitutive model. Int J Numer MethodsEng 2011;85(1):107–34.

[37] Auricchio F, Taylor RL. Shape-memory alloys: modelling and numerical simulations of the finite-strain superelastic behavior. Comput Methods Appl MechEng 1997;143(1–2):175–94.

[38] Auricchio F. A robust integration-algorithm for a finite-strain shape-memory-alloy superelastic model. Int J Plast 2001;17(7):971–90.

[39] Pethő Á. Constitutive modelling of shape memory alloys based on a finite strain description. Period Polytech Mech Eng 2000;44(1):115–26.

[40] Wang J, Moumni Z, Zhang W, Xu Y, Zaki W. A 3D finite-strain-based constitutive model for shape memory alloys accounting for thermomechanical coupling and martensite reorientation. Smart Mater Struct 2017;26(6):065006.

[41] Reese S, Christ D. Finite deformation pseudo-elasticity of shape memory alloys–constitutive modelling and finite element implementation. Int J Plast 2008;24(3):455–82.

[42] Thamburaja P. A finite-deformation-based phenomenological theory for shape-memory alloys. Int J Plast 2010;26(8):1195–219.

[43] Müller C, Bruhns O. A thermodynamic finite-strain model for pseudoelastic shape memory alloys. Int J Plast 2006;22(9):1658–82.

[44] Christ D, Reese S. A finite element model for shape memory alloys considering thermomechanical couplings at large strains. Int J Solids Struct 2009;46(20):3694–709.

[45] Stupkiewicz S, Petryk H. A robust model of pseudoelasticity in shape memory alloys. Int J Numer MethodsEng 2013;93(7):747–69.

[46] Arghavani J, Auricchio F, Naghdabadi R, Reali A, Sohrabpour S. A 3d finite strain phenomenological constitutive model for shape memory alloys considering martensite reorientation. Continuum Mech Thermodyn 2010;22(5):345–62.

[47] Zaki W. An efficient implementation for a model of martensite reorientation in martensitic shape memory alloys under multiaxial nonproportional loading. Int J Plast 2012;37:72–94.

[48] Jung Y, Papadopoulos P, Ritchie R. Constitutive modelling and numerical simulation of multivariant phase transformation in superelastic shape-memory alloys. Int J Numer MethodsEng 2004;60(2):429–60.

[49] Damanpack A, Bodaghi M, Liao W. A finite-strain constitutive model for anisotropic shape memory alloys. Mech Mater 2017;112:129–42.

[50] Souza AC, Mamiya EN, Zouain N. Three-dimensional model for solids undergoing stress-induced phase transformations. Eur J Mech-A/Solids 1998;17(5):789–806.

[51] Arghavani J, Auricchio F, Naghdabadi R, Reali A. An improved, fully symmetric, finite-strain phenomenological constitutive model for shape memory alloys. Finite Elem. Anal. Des. 2011;47(2):166–74.

[52] Wang J, Moumni Z, Zhang W, Zaki W. A thermomechanically coupled finite deformation constitutive model for shape memory alloys based on Hencky strain. Int J Eng Sci 2017;117:51–77.

[53] Wang J, Moumni Z, Zhang W. A thermomechanically coupled finite-strain constitutive model for cyclic pseudoelasticity of polycrystalline shape memory alloys. Int J Plast 2017;97:194–221.

[54] Porenta L, Kabirifar P, Žerovnik A, Čebron M, Žužek B, Dolenec M, et al. Thin-walled Ni-Ti tubes under compression: ideal candidates for efficient and fatigue-resistant elastocaloric cooling. Appl Mater Today 2020;20:100712.

[55] Artioli E, Marfia S, Sacco E, Taylor R. A nonlinear plate finite element formulation for shape memory alloy applications. Int J Numer MethodsEng 2012;89(10):1249–71.

[56] Armattoe KM, Bouby C, Haboussi M, Zineb TB. Modeling of latent heat effects on phase transformation in shape memory alloy thin structures. Int J Solids Struct 2016;88:283–95.

[57] Nodargi NA, Bisegna P. A novel high-performance mixed membrane finite element for the analysis of inelastic structures. Comput Struct 2017;182:337–53.

[58] Frischkorn J, Reese S. Solid-beam finite element analysis of nitinol stents. Comput Methods Appl MechEng 2015;291:42–63.

[59] Bisegna P, Caselli F, Marfia S, Sacco E. A new SMA shell element based on the corotational formulation. Comput Mech 2014;54(5):1315–29.

[60] Hauptmann R, Schweizerhof K, Doll S. Extension of the solid-shell concept for application to large elastic and large elastoplastic deformations. Int J Numer MethodsEng 2000;49(9):1121–41.

[61] Dvorkin EN, Bathe K-J. A continuum mechanics based four-node shell element for general non-linear analysis. Eng Comput 1984.

[62] Betsch P, Stein E. An assumed strain approach avoiding artificial thickness straining for a non-linear 4-node shell element. Commun Numer Methods Eng 1995;11(11):899–909.

[63] Kulikov G, Plotnikova S. A family of ANS four-node exact geometry shell elements in general convected curvilinear coordinates. Int J Numer MethodsEng 2010;83(10):1376–406.

[64] Ko Y, Lee P-S, Bathe K-J. A new MITC4+ shell element. ComputStruct 2017;182:404–18.

[65] Lavrenčič M, Brank B. Hybrid-mixed shell quadrilateral that allows for large solution steps and is low-sensitive to mesh distortion. Comput Mech 2020;65(1):177–92.

[66] Lavrenčič M, Brank B. Mixed low-order finite elements for geometrically exact shell models: overview and comparison. Arch Comput Methods Eng 2021. DOI: 10.1007/s11831-021-09537-2

[67] Ibrahimbegovic A. Nonlinear solid mechanics: theoretical formulations and finite element solution methods, vol 160. Springer Science & Business Media; 2009.

[68] Ibrahimbegović A. Finite elastoplastic deformations of space-curved membranes. Comput Methods Appl MechEng 1994;119(3–4):371–94.

[69] Korelc J, Stupkiewicz S. Closed-form matrix exponential and its application in finite-strain plasticity. Int J Numer MethodsEng 2014;98(13):960–87.

[70] Hudobivnik B, Korelc J. Closed-form representation of matrix functions in the formulation of nonlinear material models. Finite Elem. Anal. Des. 2016;111:19–32.

[71] Quarteroni A, Sacco R, Saleri F. Numerical mathematics, vol 37. Springer Science & Business Media; 2010.

[72] Brank B, Korelc J, Ibrahimbegović A. Nonlinear shell problem formulation accounting for through-the-thickness stretching and its finite element implementation. Comput Struct 2002;80(9–10):699–717.

[73] Brank B. Nonlinear shell models with seven kinematic parameters. Comput Methods Appl MechEng 2005;194(21–24):2336–62.

[74] Brank B, Ibrahimbegovic A, Bohinc U. On prediction of 3D stress state in elastic shell by higher-order shell formulations. CMES-Comput Model Eng Sci 2008;33(1):85–108.

[75] Brank B, Perić D, Damjanić FB. On large deformations of thin elasto-plastic shells: implementation of a finite rotation model for quadrilateral shell element. Int J Numer MethodsEng 1997;40(4):689–726.

[76] Brank B, Ibrahimbegovic A. On the relation between different parametrizations of finite rotations for shells. Eng Comput 2001.

[77] Ibrahimbegovic A, Brank B, Courtois P. Stress resultant geometrically exact form of classical shell model and vector-like parameterization of constrained finite rotations. Int J Numer MethodsEng 2001;52(11):1235–52.

[78] Brank B. Assessment of 4-node EAS–ANS shell elements for large deformation analysis. Comput Mech 2008;42(1):39–51.

[79] Simo JC, Rifai M. A class of mixed assumed strain methods and the method of incompatible modes. Int J Numer MethodsEng 1990;29(8):1595–638.

[80] Wagner W, Gruttmann F. A robust non-linear mixed hybrid quadrilateral shell element. Int J Numer MethodsEng 2005;64(5):635–66.

[81] Gruttmann F, Wagner W. Structural analysis of composite laminates using a mixed hybrid shell element. Comput Mech 2006;37(6):479–97.

[82] Korelc J, Wriggers P. Automation of finite element methods. Springer; 2016.

[83] Helm D, Haupt P. Thermomechanical behavior of shape memory alloys. In: Smart structures and materials 2001: active materials: behavior and mechanics, vol. 4333. International Society for Optics and Photonics; 2001. p. 302–13.

[84] Porenta L, Brank B, Dujc J, Brojan M, Tušek J. A shell finite element model for superelasticity of shape memory alloys. In: Analysis of shells, plates, and beams. Springer; 2020. p. 373–88.

[85] Stanić A, Brank B, Korelc J. On path-following methods for structural failure problems. Comput Mech 2016;58(2):281–306.